MINISTÉRIO DA CIÊNCIA, TECNOLOGIA E INOVAÇÕES
INSTITUTO NACIONAL DE PESQUISAS ESPACIAIS

sid.inpe.br/mtc-m21d/2022/06.03.17.28-TDI

CALIBRATION OF GNSS-TEC USING IONOSONDE DATA AND LOW LATITUDE TEC MAP GENERATION

Roberto Livy da Costa Madeira

Master's Dissertation of the Graduate Course in Space Geophysics, guided by Drs. Jonas Rodrigues de Souza, and Claudinei Rodrigues de Aguiar, approved in May 27, 2022.

URL of the original document:
<http://urlib.net/8JMKD3MGP3W34T/472R79S>

INPE
São José dos Campos
2022

PUBLISHED BY:

Instituto Nacional de Pesquisas Espaciais - INPE
Coordenação de Ensino, Pesquisa e Extensão (COEPE)
Divisão de Biblioteca (DIBIB)
CEP 12.227-010
São José dos Campos - SP - Brasil
Tel.:(012) 3208-6923/7348
E-mail: pubtc@inpe.br

MINISTÉRIO DA CIÊNCIA, TECNOLOGIA E INOVAÇÕES
INSTITUTO NACIONAL DE PESQUISAS ESPACIAIS

sid.inpe.br/mtc-m21d/2022/06.03.17.28-TDI

CALIBRATION OF GNSS-TEC USING IONOSONDE DATA AND LOW LATITUDE TEC MAP GENERATION

Roberto Livy da Costa Madeira

Master's Dissertation of the Graduate Course in Space Geophysics, guided by Drs. Jonas Rodrigues de Souza, and Claudinei Rodrigues de Aguiar, approved in May 27, 2022.

URL of the original document:
<http://urlib.net/8JMKD3MGP3W34T/472R79S>

INPE
São José dos Campos
2022

Cataloging in Publication Data

Madeira, Roberto Livy da Costa.

M264c Calibration of GNSS-TEC using ionosonde data and low latitude tec map generation / Roberto Livy da Costa Madeira. – São José dos Campos : INPE, 2022.

xviii + 60 p. ; (sid.inpe.br/mtc-m21d/2022/06.03.17.28-TDI)

Dissertation (Master in Space Geophysics) – Instituto Nacional de Pesquisas Espaciais, São José dos Campos, 2022.

Guiding : Drs. Jonas Rodrigues de Souza, and Claudinei Rodrigues de Aguiar.

1. Receiver bias. 2. Global Navigation Satellite System (GNSS). 3. Ionosonde. 4. Ionosphere. 5. Total Electron Content (TEC). I.Title.

CDU 550.388.2:629.783

MINISTÉRIO DA CIÊNCIA, TECNOLOGIA E INOVAÇÕES

INSTITUTO NACIONAL DE PESQUISAS ESPACIAIS
Serviço de Pós-Graduação - SEPGR

DEFESA FINAL DE DISSERTAÇÃO DE ROBERTO LIVY DA COSTA MADEIRA
BANCA Nº 119/2022, REG 847220/2020

No dia 27 de maio de 2022, as 15h, por teleconferência, o(a) aluno(a) mencionado(a) acima defendeu seu trabalho final (apresentação oral seguida de arguição) perante uma Banca Examinadora, cujos membros estão listados abaixo. O(A) aluno(a) foi APROVADO(A) pela Banca Examinadora, por unanimidade, em cumprimento ao requisito exigido para obtenção do Título de Mestre em Geofísica Espacial/Ciências Solar-Terrestre. O trabalho precisa da incorporação das correções sugeridas pela Banca Examinadora e revisão final pelo(s) orientador(es).

Novo Título: "CALIBRATION OF GNSS-TEC USING IONOSONDE DATA AND LOW LATITUDE TEC MAP GENERATION"

Membros da banca:

Dr. Alisson Dal Lago - Presidente - INPE
Dr. Jonas Rodrigues de Souza - Orientador - INPE
Dr. Claudinei Rodrigues de Aguiar - Orientador - UTFPR
Dr. Eurico Rodrigues de Paula - Membro Interno - INPE
Dr. João Francisco Galera Monico - Membro Externo - UNESP/PP

Documento assinado eletronicamente por **Jonas Rodrigues de Souza**, **Pesquisador**, em 30/05/2022, às 09:48 (horário oficial de Brasília), com fundamento no § 3º do art. 4º do Decreto nº 10.543, de 13 de novembro de 2020.

Documento assinado eletronicamente por **Claudinei rodrigues de Aguiar (E)**, **Usuário Externo**, em 30/05/2022, às 10:10 (horário oficial de Brasília), com fundamento no § 3º do art. 4º do Decreto nº 10.543, de 13 de novembro de 2020.

Documento assinado eletronicamente por **JOAO FRANCISCO GALERA MONICO (E)**, **Usuário Externo**, em 30/05/2022, às 10:23 (horário oficial de Brasília), com fundamento no § 3º do art. 4º do Decreto nº 10.543, de 13 de novembro de 2020.

Documento assinado eletronicamente por **Alisson Dal Lago**, **Chefe da Divisão de Heliofísica, Ciências Planetárias e Aeronomia**, em 30/05/2022, às 13:32 (horário oficial de Brasília), com fundamento no § 3º do art. 4º do Decreto nº 10.543, de 13 de novembro de 2020.

Documento assinado eletronicamente por **Eurico Rodrigues de Paula**, **Pesquisador**, em 30/05/2022, às 19:27 (horário oficial de Brasília), com fundamento no § 3º do art. 4º do Decreto nº 10.543, de 13 de novembro de 2020.

A autenticidade deste documento pode ser conferida no site http://sei.mctic.gov.br/verifica.html, informando o código verificador **9854574** e o código CRC **2EE27CA5**.

Referência: Processo nº 01340.003492/2022-11 SEI nº 9854574

ACKNOWLEDGEMENTS

I would like to thank my advisors Dr. Jonas Rodrigues de Souza and Dr. Claudinei Rodrigues de Aguiar for the patience and guidance delivered to me. Also, I thank Ângela M. Santos for the ionosonde data management.

Also, I express my gratitude to Drs. Cesar Valladares, for sharing the UTD code; Paul Wessel for sharing the MATLAB code to evaluate the Green's functions; and, Luciano Mendoza for allowing me to get access to the MAGGIA IONEX data.

I am grateful to the *Coordenação de Aperfeiçoamento de Pessoal de Nível Superior* (CAPES) for funding this work, making it possible to dedicate myself entirely in this reseach.

A great thank goes to the *National Institute for Space Research* (INPE), its professors and students, in special, my friend Amadi Brians Chinonso who helped with corrections in the sentences of this text; also, to Instituto Nacional de Ciência e Tecnologia – Tecnologia GNSS no Suporte à Navegação Aérea (INCT GNSS-NavAer) and Estudo e Monitoramento BRAsileiro de Clima Espacial (EMBRACE) program.

I also show my gratitude to the evaluation committee: Alisson Dal Lago, Eurico Rodrigues de Paula, and João Francisco Galera Monico.

Finally, I sincerely thank my family and friends outside of the INPE for all of the support given to me up to here.

ABSTRACT

Biases in *Global Navigation Satellite System* (GNSS) receivers can degrade satellite signals used for ionospheric studies. In this work, we propose the receiver bias removal using ionosonde data collected at 6.5 LT, when the ionosphere is supposed to have minimal *Total Electron Content* (TEC) gradient along magnetic longitudes of the South American sector. Also, the adapted α-Chapman function was used in order to include the plasmaspheric contribution in the ionosonde-derived TEC ($IONTEC$) calculations. For each day, a function able to describe the vertical TEC ($VTEC$) on magnetic latitudes $IONTEC(M_{Lat})$ was fitted on the ionosonde data and used to calibrate the TEC obtained from the GNSS stations of the networks *Rede Brasileira de Monitoramento Contínuo* (RBMC), *Instituto Nacional de Ciência e Tecnologia – Tecnologia GNSS no Suporte à Navegação Aérea* (INCT GNSS-NavAer), and *Système d'Observation du Niveau des Eaux Littorales* (SONEL). The estimated biases where compared to the results from the *University of Texas at Dallas* (UTD) code for TEC calibration and both have shown good agreement. Also, the coherence of the method for three consecutive days, March 21-23, 2021, a period with low solar activity, was analyzed and it has shown to be satisfactorily stable by producing the average standard deviation of the receiver bias from the RBMC network equal to 0.6376 $TECU$; a distinct case occurred at Cachoeira Paulista Station, which experienced large variation in its bias through the three days, even so, our method was able to detect an estimate of the receiver bias, ensuring the continuity of TEC data. Finally, was generated the TEC maps over the Brazilian sector and neighboring regions using minimal curvature method for interpolation and the maps were compared to the ones produced by the *Laboratorio de Meteorología Espacial, Atmósfera Terrestre, Geodesia, Geodinámica, diseño de Instrumental y Astrometría* (MAGGIA laboratory). It was noticed that just the maps generated with our method were able to detect properly *Equatorial Plasma Bubble* (EPB) signatures, such that these signatures were also identified by All-Sky imager pictures and $S4$ data.

Palavras-chave: Receiver bias. Global Navigation Satellite System (GNSS). Ionosonde. Ionosphere. Total Electron Content (TEC).

CALIBRAÇÃO DO GNSS-TEC USANDO DADOS DE IONOSSONDA E GERAÇÃO DE MAPAS DE TEC EM BAIXAS LATITUDES

RESUMO

Erros em receptores de *Global Navigation satellite System* (GNSS) podem corromper sinais de satélites usados para estudos da ionosfera. Neste trabalho, nós propomos a remoção de tendências de receptores usando dados de ionossonda coletados às 6.5, hora local, quando se supõe que a ionosfera tem gradiente mínimo no *Conteúdo Eletrônico Total* (TEC) em longitudes magnéticas no setor Sul-americano. Usou-se a função Chapman-α adaptada de tal maneira a incluir as contribuições da plasmasfera no cálculo do TEC derivado de ionossonda (IONTEC). Para cada dia, uma função capaz de aproximar o TEC vertical ($VTEC$) em latitudes magnéticas ($IONTEC(M_{Lat})$) foi ajustada nos dados de ionossondas e usada para calibrar os valores de TEC obtidos com as informações dos receptores GNSS da *Rede Brasileira de Monitoramento Contínuo* (RBMC); e, redes do *Instituto Nacional de Ciência e Tecnologia – Tecnologia GNSS no Suporte à Navegação Aérea* (INCT GNSS-NavAer) e *Système d'Observation du Niveau des Eaux Littorales* (SONEL). As tendências estimadas foram comparadas às obtidas pelo código *University of Texas at Dallas* (UTD) de calibração de TEC, onde ambos mostraram boa concordância. Também foi investigada a coerência do método para três dias consecutivos de baixa atividade solar, 21-23/03/2021, o qual se mostrou satisfatoriamente estável com um desvio padrão médio para as tendências dos receptores RBMC igual a 0.6376 $TECU$; um caso peculiar ocorreu na estação de Cachoeira Paulista, à qual experimentou grande variação nas suas tendências nos três dias analisados, mesmo assim, nosso método foi capaz de detectar e estimar o valor correto, garantindo a continuidade dos dados de TEC. Finalmente, foram gerados mapas de TEC sobre o setor brasileiro e regoões vizinhas através de interpolação com método da curvatura mínima e comparados com os mapas do *Laboratorio de Meteorología Espacial, Atmósfera Terrestre, Geodesia, Geodinámica, diseño de Instrumental y Astrometría* (MAGGIA), onde apenas os mapas gerados pelo nosso método foram capazes de detectar propriamente assinaturas de *Bolhas de Plasma Equatoriais* (EPBs), onde tais assinaturas também foram identificadas por imageadores All-Sky e dados de índice $S4$.

Palavras-chave: Erros de receptor. Global Navigation Satellite System (GNSS). Ionossonda. Ionosfera. Conteúdo Eletrônico Total (TEC).

LIST OF FIGURES

Page

LIST OF TABLES

Page

LIST OF ABBREVIATIONS

CADI	–	Canadian Advanced Digital Ionosonde
C/A	–	Coarse Acquisition code
DCB	–	Differential Code Bias
DPB	–	Differential Phase Bias
DIHPA	–	DIvision of Heliophysics Planetary sciences and Aeronomy
EIA	–	Equatorial Ionization Anomaly
EPB	–	Equatorial Plasma bubble
EUV	–	Extreme Ultra Violet
GNSS	–	Global Navigation Satellite System
GNSS-NavAer	–	Tecnologia GNSS no Suporte à Navegação Aérea
GPS	–	Global Positioning System
HF	–	High Frequency
IBGE	–	Instituto Brasileiro de Geografia e Estatística
INCT	–	Instituto Nacional de Ciência e Tecnologia
INPE	–	National institute for Space Research
IONEX	–	IONosphere map EXchange
IONTEC	–	Ionosonde-derived TEC
IPP	–	Ionospheric Pierce Point
LT	–	Local Time
MAGGIA	–	Laboratorio de Meteorología Espacial, Atmósfera Terrestre, Geodesia, Geodinámica, diseño de Instrumental y Astrometría
PRN	–	PseudoRandom Noise code
PVT	–	Positioning, Velocity and Time
RBMC	–	Rede Brasileira de Monitoramento Contínuo dos sistemas GNSS
RINEX	–	Receiver Independent Exchange Format
SAO	–	Standard Archive Output Format
SBAS	–	Satellite Based Augmentation System
SLIM	–	Single Layer Ionosphere Model
SONEL	–	Système d'Observation du Niveau des Eaux Littorales
STEC	–	Slant TEC
TEC	–	Total Electron Content
TECU	–	TEC Unity
UT	–	Universal Time
UTD	–	University of Texas at Dallas

CONTENTS

1 INTRODUCTION

Global Navigation Satellite Systems (GNSS) are high technology systems used for positioning and also for ionospheric research. However, data provided by GNSS receivers are often contaminated by biases, which can reduce the measurement accuracy. According to Vierinen et al. (2016), these biases, also known as instrumental effects, arise from dispersive hardware components in the transmitter and receiver, causing signal delays, which are dependent on the frequencies. Another time delay that occurs in GNSS signal broadcasting is due to the refractive property of the region known as *ionosphere*. The ionosphere is the ionized part of the upper atmosphere, which is composed of a significant number of free electrons and positive ions, with negative ions predominant in its lower altitudes (HARGREAVES, 1992; PRÖLSS, 2012). The group delay and phase advancement due to ionosphere are in the same magnitude and opposite sign between them; also, in a first approximation, both are proportional to the electron summation between the receiver and satellite in one square meter column and inversely proportional to the square of the transmission frequency (HOFMANN-WELLENHOF et al., 2007; OTSUKA et al., 2002; PAJARES et al., 2005). The previously mentioned summation is known as *Total Electron Content* (TEC) and can be represented by the following integral:

$$TEC = \int_{receiver}^{satellite} N ds, \tag{1.1}$$

where N is the electron density and ds is the infinitesimal distance between the satellite and the receiver. As TEC can assume large values, it is better expressed in TEC units ($TECU$), being 1 $TECU = 10^{16} electrons \cdot \mathrm{m}^{-2}$.

Several works have been published showing how the GNSS receiver bias can be removed, e.g. Carrano and Groves (2006); Otsuka et al. (2002); Rideout and Coster (2006); Themens et al. (2013); Vierinen et al. (2016). If the *Global Positioning System* (GPS) constellation is considered, which transmits signals on three carrier frequencies, L_1, L_2, and L_5, also if the instrumental effects are correctly removed and a sufficient number of satellites are viewed by the receiver, one can obtain information about the ionosphere and accurate position by combining observables obtained from L_1, L_2, and L_5. However, TEC estimations in the equatorial ionosphere become a challenge due to spatio-temporal density gradients and satellite signal scintillation (CARRANO; GROVES, 2006). Also, according to Themens et al. (2013), these previous methods may not offer accuracy, at least in high latitudes, where some prior conditions cannot be assumed.

In this work, we propose receiver bias removal using data from *ionosondes*. An ionosonde is a device used for ionospheric sounding; it works like radar emitting pulses into the vertically up direction and measuring the time of response. By sweeping in a spectrum of frequencies, a vertical frequency profile is generated up to the height (h_mF_2) where occurs the maximum ionospheric plasma frequency (f_mF_2). The stored profile is named *ionogram* and it represents the ionospheric plasma frequency in function of a virtual height.

The motivation of this study arises from the necessity of a precise TEC database for ionospheric research, GNSS navigation, and HF communication in the equatorial and low latitude ionosphere, where a large response to extreme magnetic conditions, strong spatio-temporal gradients, and several irregularities are found. Therefore, a method for GNSS bias removal is worth studying. We have applied our method for three consecutive days 21, 22, and 23 of March 2021, in a transition period from geomagnetically moderate to calm. We collected data from ionosondes available at *Estudo e Monitoramento BRAsileiro de Clima Espacial* (EMBRACE) at Instituto Nacional de Pesquisas Espaciais (INPE) (2021) or at *DIvision of Heliophysics, Planetary science and Aeronomy* (DIHPA) also at INPE; the TEC from ionograms were calculated using the adapted α-Chapman function (JAKOWSKI, 2005) to model the top of the ionosphere; the ionosonde stations were tagged in magnetic latitudes and the TEC latitudinal distribution was generated by polynomial fitting. Finally, we produce the TEC maps using the minimum curvature approach for interpolation (PARKER, 1994; WESSEL; BECKER, 2008).

This work is divided into five chapters. In Chapter 2, we describe briefly the theory of wave propagation through magnetoionic mediums, such as the ionosphere, discuss some ionospheric properties like its topology, basic chemistry and dynamics, and conclude with a description of the action of such region upon radio waves.

Chapter 3 is dedicated to the methodology with an emphasis on the radio techniques used in this work for ionospheric probing: the *Global Positioning System* (GPS) and the main features of an ionosonde/DIGISONDE. Further, some existing methods for receiver bias removal are discussed in order to justify and illustrate our research. The chapter is concluded with an explanation of our method for calibration and TEC map generation.

In Chapter 4, we show our results and compare the receiver bias estimations with the results from the UTD code for TEC calibration, which was kindly provided by Cesar Valladares, and the day-to-day variation of the measurements for the three

days are discussed. Consecutively, using the calibrated TEC data, we show how an interpolation function was applied to generate a distribution of TEC mainly over the Brazilian sector to be compared with TEC maps generated by Mendoza et al. (2020) followed by a qualitative comparison with pictures of all-sky imagers available at Instituto Nacional de Pesquisas Espaciais (INPE) (2021).

Finally, in Chapter 5, we conclude by summarizing our method and achievements; also, some future improvements are listed.

2 WAVE PROPAGATION IN THE IONOSPHERE

In free space, an electromagnetic wave travels at velocity c (the velocity of light). However, if the signal crosses an ionized medium, the refractive index is no longer 1 and the wave suffers a delay in its velocity and advancement in phase. It is worth noting that even if the phase travels faster than c, no information is carried, maintaining the relativistic principles (HOFMANN-WELLENHOF et al., 2007; PAJARES et al., 2005). According to Hofmann-Wellenhof et al. (2007), the refractive index depends on water vapor, temperature, pressure, signal frequency, and the number of free electrons. The ionosphere is a dispersive medium even at 1.5 GHz, thus, waves with different characteristics have different phase velocities while crossing this region. Therefore, it is a matter of interest to describe some general ionospheric properties.

2.1 The ionosphere

In the modern world, one of the most important space area worth studying is the region called *ionosphere*. It is of good agreement that it is located mainly between 50 and 1000 km of altitude. Such region, sometimes referred as a layer, is composed of positive ions and electrons, behaving as plasma. With the emergence of the civilian operations of satellite technologies, the understanding and modeling of the ionosphere are matters of great importance. In respect to the *radio waves*, or *electromagnetic waves* in general, this atmospheric region can work as a dielectric or a metallic reflector, depending on the radio wave frequency (PRÖLSS, 2012).

According to Rishbeth (1969), the existence of a conducting layer was suggested previously to explain small daily variations in the geomagnetic field. Some authors defend that C. F. Gauss in 1939 attributed these fluctuations to atmospheric currents. In 1901, G. Marconi did a successful experiment, which transmitted radio signal across the Atlantic and showed that the waves were much more likely deflected than refracted. In the following year, 1902, A. E. Kennelly and O. Heaviside suggested that this kind of reflective behavior would be due to free electric charges in the upper atmosphere (RISHBETH, 1969).

The term, *"ionosphere"*, of course, refers to the high ion density in that region and, assuming macroscopic neutrality, a similar electron density for each ion density profile is obtained, which can vary from 10^3 to 10^6 cm^{-3}. The previous assumption is reasonable above 90 km altitude (PRÖLSS, 2012). The high ion-electron density in this layer is strongly related to the solar-terrestrial interactions, also, it presents a stratified behavior. The ionosphere subdivision is best represented by its verti-

cal plasma density variations in contrast to the neutral atmosphere which is more conveniently characterized by its temperature distribution (KELLEY, 2009). Figure 2.1 represents typical values of the atmosphere in terms of temperature and plasma density; the left side profile stands for the neutral atmosphere subdivision and the right side graphic represents the plasma density during the daytime (solid line) and nighttime (dashed line).

Figure 2.1 - Neutral and ionized atmosphere.

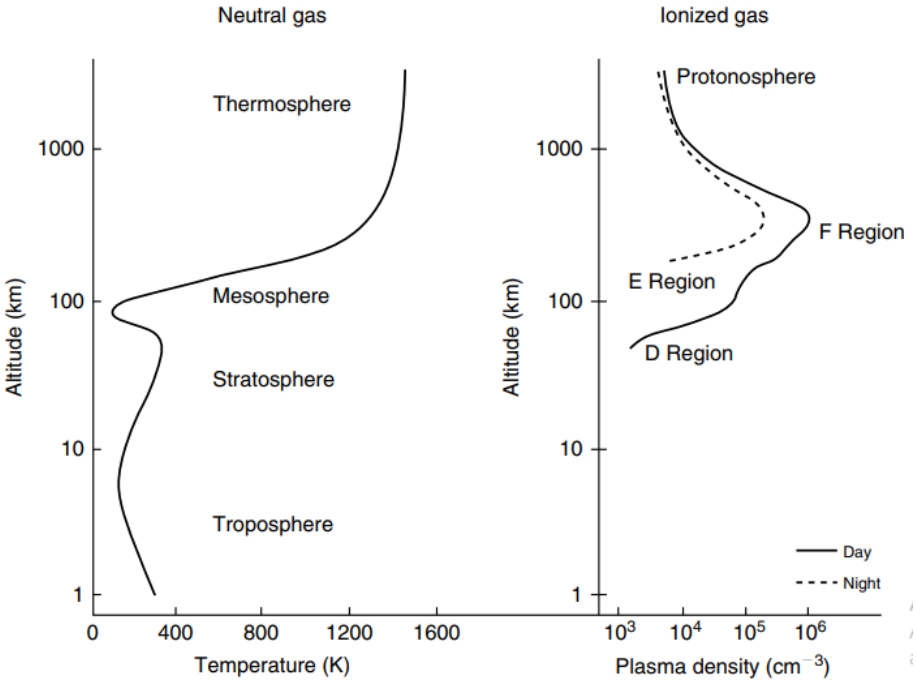

Typical temperature and plasma density profile in the atmosphere.
SOURCE: Kelley (2009).

Prölss (2012) presented a subdivision, Table 2.1, related to the predominant ion distribution as D, E, and F regions, which are, respectively, dominated by the cluster and negative ions under 90 km; O_2^+ and NO^+ approximately between 90 – 170 km; and O^+ between 170 – 1000 km. Above these layers (approx. over 1000 km), the region dominated by H^+ is named *plasmasphere*.

The maximum electron density occurs in the F region and it is called F_2 peak. A subscript is used to split the F region into F_1 and F_2 regions. The reason behind that is because, in the daytime, another electron density peak (but not global) appears

Table 2.1 - Classification of the ionosphere according to composition.

Ionosphere	D region	$h \lesssim 90$ km	$H_3O^+ \cdot (H_2O)_n$, NO_3^-
	E region	$90 \lesssim h \lesssim 170$ km	O_2^+, NO^+
	F region	$170 \lesssim h \lesssim 1000$ km	O^+
Plasmasphere		$h \gtrsim 1000$ km	H^+

SOURCE: Adapted from Prölss (2012).

over the F_2 peak. Also, a sporadic occurrence of the so-called F_3 layer has been noted and studied (BALAN; BAILEY, 1995; BATISTA et al., 2002). Still according to Batista et al. (2002), the sporadic F_3 layer would be formed due to $\mathbf{E} \times \mathbf{B}$ drift around the magnetic equator combined with the magnetic meridional neutral wind, which provides an upward plasma drift near and below the F_2 peak, during noon periods, as predictable by ionospheric models.

2.1.1 The ionization production and loss

The ionized region is nothing but the neutral upper part of the atmosphere which received energy from the sun enough to decouple ion/positive-molecules and electrons, whose dynamics (movements) are driven by neutral winds and controlled by the magnetic field (BALAN et al., 2018). According to Hargreaves (1992), the concentration of free electrons in the ionosphere is related in Equation 2.1,

$$\frac{\partial N_e}{\partial t} + \nabla \cdot (N_e \mathbf{v}) = q - L, \tag{2.1}$$

which is the continuity equation for the electron density N_e with dynamic changes due to $N_e\mathbf{v}$, where $\mathbf{v}$ is the mean drift velocity and rates of production and loss given by q and L respectively. Three main factors contribute for the term q in 2.1. The absorption of solar energy in Extreme Ultra Violet (EUV) and X-ray band generates photoionization in the ionosphere, and it is called primary photoionization; the secondary ionization process is related to photoelectrons and scattered or reemitted radiation; the third process plays an important role in polar regions and it arises from the precipitation of energetic particles (PRÖLSS, 2012). The main loss processes are related to recombination, which can occur due to other several factors.

Some details about the main ionization production processes are:

- the *primary photoionization*, a nondissociative process represented as

(PRÖLSS, 2012)

$$\mathrm{X} + \mathrm{ph}(\lambda \lesssim 100 \text{ nm}) \longrightarrow \mathrm{X}^+ + \mathrm{e}$$

where X^+ is a molecule or atom, ph represents a photon with wavelength λ and e is the electron generated by the processes;

- the *secondary ionization processes*, which is due to photoelectrons released in the primary ionization; and,
- the *ionization by energetic particles*. This ionization process is important in high latitudes in celestial bodies whose magnetic fields have dipolar characteristic (HARGREAVES, 1992; KIVELSON et al., 1995). This phenomenon has the form (PRÖLSS, 2012)

$$\mathrm{X} + \mathrm{e}_p(E \gtrsim 12 \text{ eV}) \longrightarrow \mathrm{X}^+ + \mathrm{e}_p + \mathrm{e}_s,$$

where E is the energy of an precipitating electron, the index p is for the primary precipitating electron and s is for the new (secondary) produced electron.

In respect to the term L in 2.1, we can summarize the electron loses in the ionosphere as (KIVELSON et al., 1995; PRÖLSS, 2012)

- the *radiative recombination*,

$$\mathrm{X}^+ + \mathrm{e} \longrightarrow \mathrm{X} + \mathrm{ph};$$

- the *dissociative recombination*,

$$\mathrm{XY}^+ + \mathrm{e} \longrightarrow \mathrm{X} + \mathrm{Y};$$

- the *attachment*,

$$\mathrm{Z} + \mathrm{e} \longrightarrow \mathrm{Z}^-;$$

being X, Y and Z atoms or molecules.

2.1.2 Electron density peak

The electron density peak occurs in the F_2 region and has great importance in the ionospheric analysis. To understand the formation of this maximum, consider the

simplest ionosphere modeling, which consists of the absorption of a monochromatic radiation by a planar isothermal ionosphere, composed of single gas species, X. The number of photons absorbed per units of volume and time is given by (PRÖLSS, 2012)

$$\frac{dN_{ph}}{dV\,dt} = \sigma_{\mathrm{X}}^{A} n_{\mathrm{X}} \phi^{ph}, \tag{2.2}$$

where $\phi^{ph} = \phi_{\infty}^{ph} e^{-\tau}$ is the photon flux, ϕ_{∞}^{ph} is the photon flux outside of the Earth's atmosphere, τ is the optical depth, n_{X} is the X species density and σ_{X}^{A} its absorption cross-section. The absorbed photons can also dissociate molecules or generate excitation. Considering the fraction of photons that was responsible just for the ionization η_{X}^{I} (ionization efficiency), the volumetric and temporal rate variation of the number of ions, $q_{\mathrm{X}^+}^{PI}$, in 2.2 generated by primary ionization is

$$q_{\mathrm{X}^+}^{PI} = \eta_{\mathrm{X}}^{I} \sigma_{\mathrm{X}}^{A} n_{\mathrm{X}} \phi^{ph} = \sigma_{\mathrm{X}}^{I} n_{\mathrm{X}} \phi^{ph}, \tag{2.3}$$

where σ_{X}^{I} is the *ionization cross-section*. Figure 2.2 represents the behavior of the main gas density, which decreases with height, and the solar radiation intensity, increasing with height, both governing the primary ion production rate. At the h_{max} altitude, the radiation is still enough to produce a large amount of ionization before the concentration becomes too small; at this point, the peak of electron density occurs.

Also, if we consider that the ionospheric model in 2.3 satisfies the additional following properties: X has an exponential distribution with scale height constant and no horizontal gradients, it is known as *Chapman production function* and can be written as (HARGREAVES, 1992; KIVELSON et al., 1995; PRÖLSS, 2012; RISHBETH, 1969)

$$q = q_{m0} \exp(1 - z - \sec\chi \cdot e^{-z}), \tag{2.4}$$

where $z = (h_{m0} - h)/H$ is the reduced height for the neutral species, H is the scale height, χ is the zenith angle, h_{m0} is the height of maximum production for $\chi = 0$, and q_{m0} is the production rate at h_{m0}. Figure 2.3 shows the behavior of the normalized Chapman production function versus reduced height for various zenith angles. 2.4 will play an important role in our further discussions. The Chapman function and its variations are often used to model topside ionosphere in ionosonde-derived data. Such data are used for ionospheric research and are useful for several nowadays applications. The ionosphere alters significantly the properties of an electromagnetic wave passing through such a region. In the next section, we present some of those

Figure 2.2 - Ionization layer.

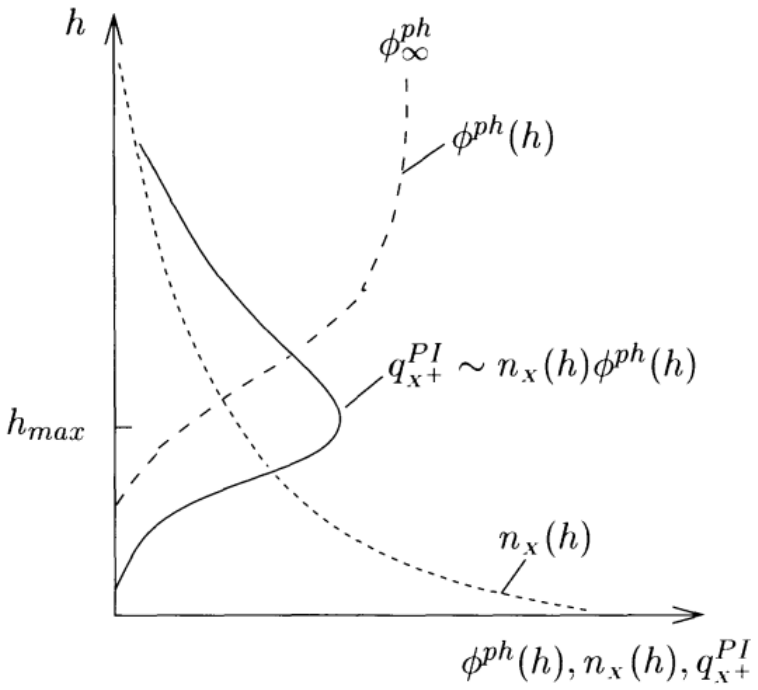

SOURCE: Prölss (2012).

effects.

2.2 Radio wave propagation in the ionosphere

Every electromagnetic wave crossing the ionosphere or any ionized medium undergoes changes in its propagation direction, amplitude, and velocity. The study of ionized medium and radio waves interaction is known as *magnetoionic theory*. In general, the refractive index for an ionized medium is (HARGREAVES, 1992; RISHBETH, 1969)

$$n^2 = 1 - \frac{X}{1 - iZ - \left[\frac{Y_T^2}{2(1-X-iZ)}\right] \pm \left[\frac{Y_T^4}{4(1-X-iZ)^2} + Y_L^2\right]^{1/2}}, \tag{2.5}$$

where i is the imaginary unity, X, Y and Z are dimensionless magnetoionic param-

Figure 2.3 - Normalized Chapman function.

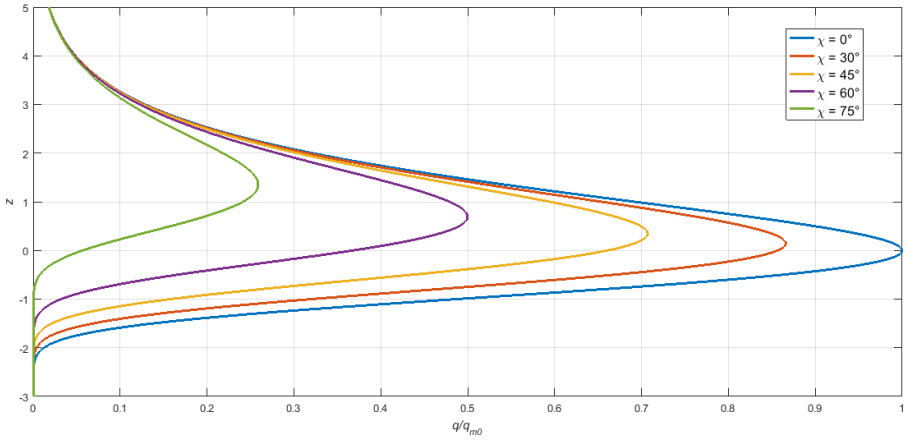

Normalized Chapman function for various zenith angles.
SOURCE: The author.

eters given by

$$\begin{cases} X = \omega_N^2/\omega^2 \\ Y = \omega_B/\omega \\ Y_L = \omega_L/\omega \\ Y_T = \omega_T/\omega \\ Z = \nu/\omega \end{cases}$$

being ω_N, ω_B, ω_L, ω_T, ω and ν, respectively, the angular plasma frequency, the electron gyro frequency, the longitudinal and transverse components of ω_B, the wave angular frequency and the frequency of collision (HARGREAVES, 1992).

Equation 2.5 is known as *Appleton-Hartree equation* and neglecting the geomagnetic field effects, considering that the absorption is small, 2.5 reduces to

$$n_{ph}^2 = 1 - \frac{\omega_N^2}{\omega^2}, \tag{2.6}$$

where the subscript ph is to name this as *phase refractive index*. Still according to the same assumption, the *group refractive index* is given by $n_{gr} = 1/n_{ph}$ (SCOTTO et al., 2012). It is easy to see that for $\omega_N > 0$, $n_{ph} < 1$ and $n_{gr} > 1$, and both refractive

indexes are related the group and phase velocities v_{gr} and v_{ph} as

$$v_{gr} = \frac{c}{n_{gr}} \tag{2.7a}$$

$$v_{ph} = \frac{c}{n_{ph}}. \tag{2.7b}$$

It means that for an electromagnetic wave crossing a plasma region like the ionosphere, the reflection will occur at the altitude where $\omega_N = \omega$, i.e. where/when $n_{gr} = 0$[1]. This property is used for vertical ionospheric sounding by ionosondes.

The aforementioned inequalities for the refractive indexes and the equations 2.7a and 2.7b allow us to write

$$\begin{aligned} n_{gr} > 1 > n_{ph} \\ \frac{1}{n_{gr}} < 1 < \frac{1}{n_{ph}} \\ \frac{c}{n_{gr}} < c < \frac{c}{n_{ph}} \\ v_{gr} < c < v_{ph}. \end{aligned} \tag{2.8}$$

Therefore, if the carrier frequency is larger than the maximum ionospheric plasma frequency, the signal will not be reflected and will change according to the ionosphere properties in such way that the signal will suffer a delay in group velocity and advancement in phase velocity as seen in the last inequality of 2.8. Figure 2.4 shows the behavior of the phase and group velocities in function of their angular frequency ω in an isotropic plasma, whose frequency is ω_N; note that the inequality 2.8 is verified, and also, it is in agreement with the physical basis, because for extremely high frequencies ($\omega >> \omega_N$), even the electrons are not able to respond to an oscillating electric field (BITTENCOURT, 2004), the refractive indexes tend to 1; consequently, the group and phase velocities tend to c.

The equivalent ionospheric phase and group effects in the unity of meters are given by (HOFMANN-WELLENHOF et al., 2007)

$$I_{ph} = -\frac{40.3}{f^2} \int N_e ds = -\frac{40.3}{f^2} TEC \tag{2.9}$$

[1]The signal travels at group velocity.

Figure 2.4 - Phase and group velocities in a plasma.

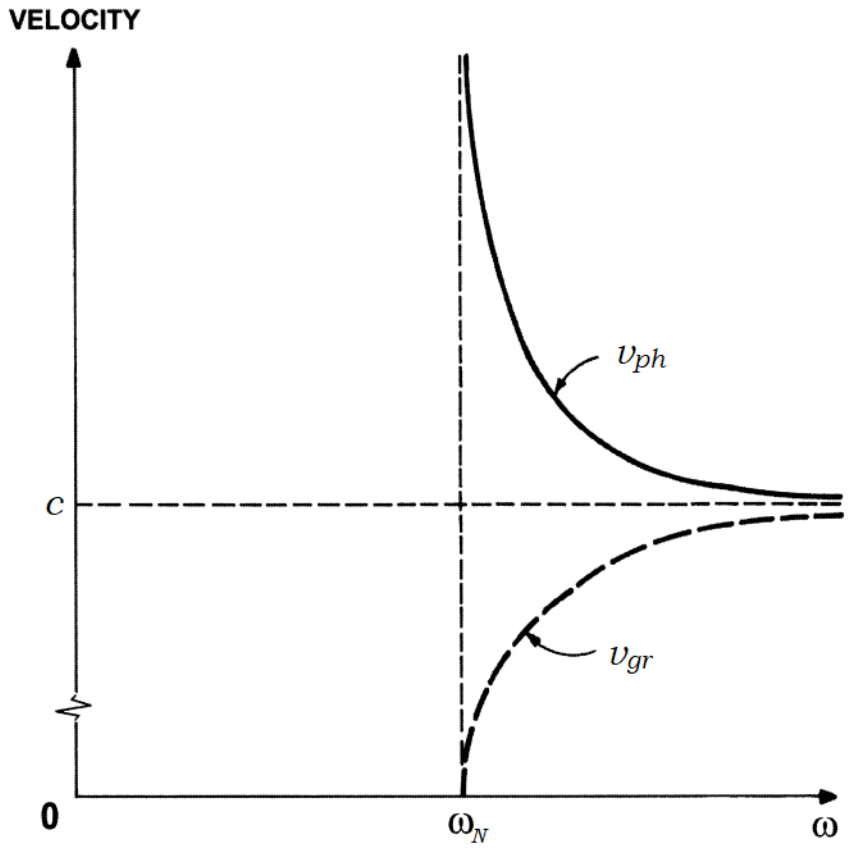

Behavior of v_{gr}, dashed line, and v_{ph}, solid line, depending on their angular frequency ω in an isotropic plasma with angular frequency ω_N.

SOURCE: Adapted from Bittencourt (2004).

$$I_{gr} = \frac{40.3}{f^2} \int N_e ds = \frac{40.3}{f^2} TEC. \tag{2.10}$$

The integral

$$TEC = \int_{receiver}^{satellite} N_e ds \tag{2.11}$$

is the total electron content in a circular column with a cross-sectional area of 1 m^2 between the signal emitter and receiver; its geometry is schematically represented in Figure 2.5, where the emitter is a satellite and the receiver is some GNSS antenna over the Earth's surface. Also, TEC is usually given in $TECU$ (TEC unity), where $1 TECU = 10^{16} electrons/\mathrm{m}^2$.

Figure 2.5 - Total Electron Content (TEC).

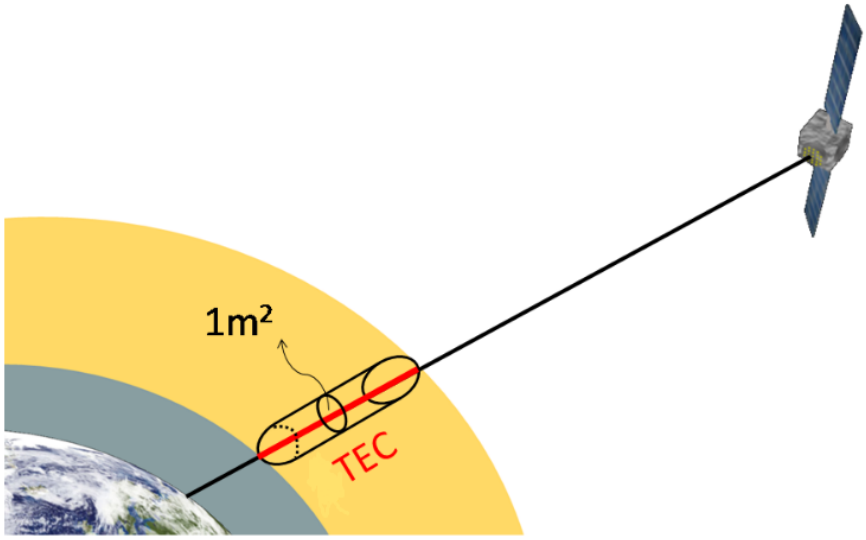

SOURCE: Adapted from Royal Observatory of Belgium (ROB) (2008).

As we mentioned before, the magnetoionic theory will help us to identify ionospheric parameters and their behaviors in order to improve the understanding of such region. In the next chapter, we introduce the main concepts of the two techniques used in this work for ionospheric sounding, the ionosonde technique and the Global Positioning System (GPS), a particular Global Navigation Satellite System.

3 METHODOLOGY

3.1 Radio techniques for ionospheric probing

In this work, we will concern with the ionospheric sounding via the Global Positioning System (GPS) and ionosonde of the DIGISONDE type.

3.1.1 The Global Positioning System

The *Global Positioning System* (GPS) is a constellation of at least 24 satellites orbiting the Earth at about 20,200 km of altitude, transmitting continuous signals for three-dimensional positioning, velocity, and time (PVT) determination (PAJARES et al., 2005). If a satellite s and a receiver r are in the same reference system, the geometric distance between them is given by

$$\rho_r^s = ||\boldsymbol{\rho}^s - \boldsymbol{\rho}_r||, \tag{3.1}$$

where $\boldsymbol{\rho}_r$ is the receiver position (moving or fixed) and $\boldsymbol{\rho}^s$ is the satellite position in the considered system of reference.

To have a basic idea of (GPS) positioning, consider the illustrative two-dimensional case in Figure 3.1. Assuming that we know the coordinates of a lighthouse emitting acoustic signals in intervals of 1 min. Also, supposing that it starts to emit at 0 hours, 0 minutes, 0 seconds and a ship far away from the lighthouse with a perfect synchronized clock detects this signal in a time interval different from a multiple of 1 minute, for example, 20 sec later ($t = n \cdot 1m + 20s$). Thus, these 20 seconds are due to the propagation of the sound. The distance between the receiver (ship) and the emitter (lighthouse) will be the time of propagation times the velocity of sound. However, a circumference of ambiguity will appear, as presented in Figure 3.1. If there is another lighthouse, the ambiguity will reduce to two points, which is the intersection of the two circumferences. Finally, the coordinate can be uniquely determined if a third lighthouse is added (PAJARES et al., 2005). This example illustrates the case of GPS. In the GPS system, the geometry is in three dimensions and the propagating signal is an electromagnetic wave. In the previous example, was supposed a synchronism between transmitter and receiver. In practice, it does not occur (PAJARES et al., 2005). Figure 3.2 illustrates what happens when there is no synchronization of clocks. The intersection of the three circumferences will not occur in just a single point, but in a region of uncertainty, where the real position must be.

Figure 3.1 - Ambiguity in Position.

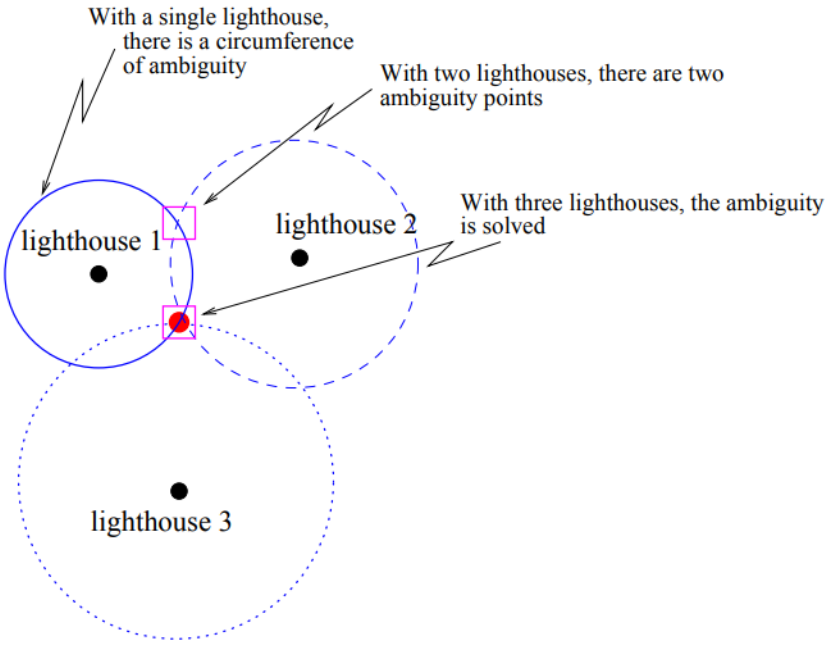

SOURCE: Pajares et al. (2005).

To assure stability in the clock, the satellites contain an atomic oscillator with daily stability of about 10^{-13} $(\Delta f/f)$[1] and the receivers are usually equipped with quartz clocks with poorer stability (PAJARES et al., 2005).

Figure 3.3 shows an illustration of triangulation in three dimensions for a user viewing three satellites.

The GPS satellites transmit signals centered in two L band frequencies, which are derived from a fundamental frequency $f_0 = 10.23$ MHz, generated by its atomic clock (HOFMANN-WELLENHOF et al., 2007; PAJARES et al., 2005). The frequencies are

$$L_1 = 154 \times 10.23 \text{ MHz} = 1575.42 \text{ MHz}$$

$$L_2 = 120 \times 10.23 \text{ MHz} = 1227.60 \text{ MHz},$$

and it allows to avoid the ionospheric refraction errors due to TEC in the ionospheric free combination. Also, a third carrier frequency called L_5 is broadcast by GPS

[1]The time required to this oscillator deviate 1 second is 300,000 years

Figure 3.2 - Clock Error Effect.

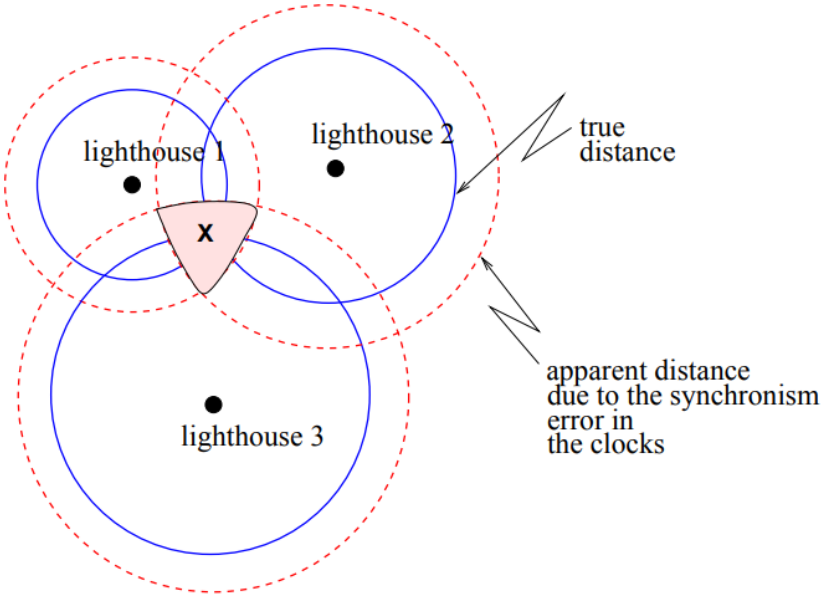

SOURCE: Pajares et al. (2005).

satellite; here, we just concern with L_1 and L_2, and their respective observables.

3.1.2 Observables

The most used observables for TEC calculations are the *code pseudorange* P, modulated on L_1 and L_2; the *coarse/acquisition code* C/A, modulated just upon L_1; and, *carrier phase* Φ in respect to L_1 and L_2, measured directly from the received signal. P is referred to as pseudorange observable due to clock and propagation errors, which alter the measured length between receiver and satellite. As shown in Figure 3.4, such errors are related to propagation in the atmosphere, relativistic effects, multipath, etc.

According to Themens et al. (2013), also neglecting multipath effects and considering that the relativistic corrections are done, the code (pseudorange) modulated on L_1 and L_2 and carrier phase measurements for the receiver i and satellite j, in meters,

Figure 3.3 - Triangulation.

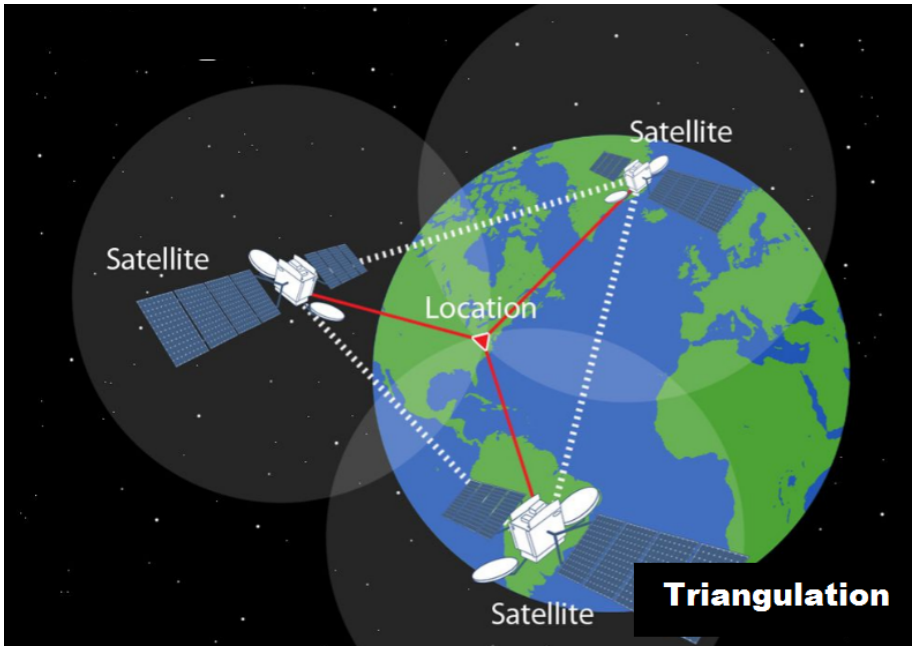

SOURCE: Adapded from Zapella et al. (2018).

are

$$P_1 = \rho_i^j + c(dt^j - dt_i) + T_i^j + I_{i,1,P}^j + c(d_{i,1} + d_1^j) \quad (3.2a)$$

$$P_2 = \rho_i^j + c(dt^j - dt_i) + T_i^j + I_{i,2,P}^j + c(d_{i,2} + d_2^j) \quad (3.2b)$$

$$\Phi_1 = \rho_i^j + c(dt^j - dt_i) + T_i^j + I_{i,1,\Phi}^j + c(\phi_{i,1} + \phi_1^j) + \lambda_1 N_{i,1}^j \quad (3.2c)$$

$$\Phi_2 = \rho_i^j + c(dt^j - dt_i) + T_i^j + I_{i,2,\Phi}^j, + c(\phi_{i,2} + \phi_2^j) + \lambda_2 N_{i,2}^j \quad (3.2d)$$

where c is the speed of light in vacuum, ρ_i^j is the geometric distance between satellite j and receiver i, dt^j and dt_i are, respectively, satellite and receiver clock errors, $I_{i,L,P}^j$ and $I_{i,L,\Phi}^j$ are ionospheric code error for pseudorange and phase on L_1 and L_2 (as defined in equations 2.10 and 2.9, respectively), T_i^j is the tropospheric error, $d_{i,L}$ and d_L^j are receiver and satellite hardware errors in code on L_1 and L_2, $\phi_{i,L}$ and ϕ_L^j are the same error for carrier phase measurements and, finally, λ_L and $N_{i,L}^j$ are, respectively, the wavelength and phase ambiguity for L_1 and L_2.

3.1.3 TEC from GPS observables

Taking the difference $P^j_{i,I} = P_2 - P_1$ (the code ionospheric observable) in Equations 3.2a and 3.2b, as well as $\Phi^j_{i,I} = \Phi_1 - \Phi_2$ (the phase ionospheric observable) in 3.2c and 3.2d, we cancel out all of the terms which do not depend on the frequencies. We are left with

$$P^j_{i,I} = I^j_{i,2,P} - I^j_{i,1,P} + c(DCB^j + DCB_i) \tag{3.3a}$$

$$\Phi^j_{i,I} = I^j_{i,1,\Phi} - I^j_{i,2,\Phi} + c(DPB^j + DPB_i) + n^j_i, \tag{3.3b}$$

where

$$\begin{cases} n^j_i = \lambda_1 N^j_{i,1} - \lambda_2 N^j_{i,2} \\ DCB^j = d^j_2 - d^j_1 \\ DCB_i = d_{i,2} - d_{i,1} \\ DPB^j = \phi^j_1 - \phi^j_2 \\ DPB_i = \phi_{i,1} - \phi_{i,2}. \end{cases}$$

In 3.3a and 3.3b, DCB and DPB are, respectively, for *differential code bias* and *differential phase bias* in satellite j and receiver i. Note also that they have units of seconds. The terms $I^j_{i,L,P}$ and $I^j_{i,L,\Phi}$ are given in, Equations 2.10 and 2.9, as it was mentioned before; that is,

$$I^j_{i,f,P} = -I^j_{i,f,\Phi} = \frac{40.3}{f^2} STEC^j_i, \tag{3.4}$$

Figure 3.4 - Errors in pseudorange measurements.

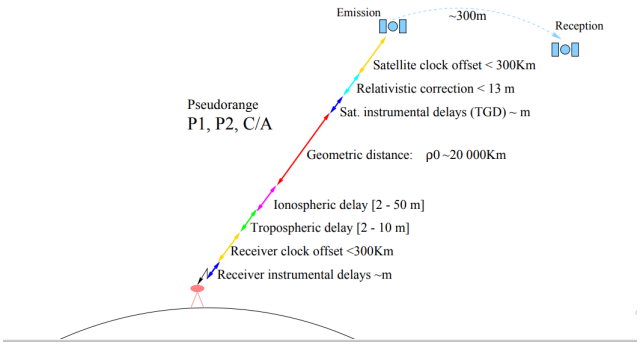

The main errors is on pseudorange measurements from C/A and P codes. SOURCE: Pajares et al. (2005).

where we named L by f (in Hz) for simplicity and $STEC$ is the slant TEC, the total electron content along the geometric distance between receiver and satellite, represented in Figure 3.7. By combining 3.3a and 3.3b with 3.4, we obtain

$$P_{i,I}^{j} = 40.3\left(\frac{f_1^2 - f_2^2}{f_1^2 f_2^2}\right) STEC_i^j + c(DCB^j + DCB_i) \tag{3.5a}$$

$$\Phi_{i,I}^{j} = 40.3\left(\frac{f_1^2 - f_2^2}{f_1^2 f_2^2}\right) STEC_i^j + c(DPB^j + DPB_i) + n_i^j. \tag{3.5b}$$

The $STEC$ measured from pseudorange, Equation 3.5a, does not have phase ambiguity but it is extremely noisy, whereas $STEC$ by 3.5b is more precise, even it carriers the ambiguity term (CARRANO; GROVES, 2006; THEMENS et al., 2013). Therefore, a process called *phase leveling* (THEMENS et al., 2013) is performed. Such process levels the phase derived $STEC$ to the one derived from pseudorange. We define the leveling constant as follows:

$$W = \frac{1}{N_{arc}} \sum_{n=1}^{N_{arc}} (P_{i,I}^{j} - \Phi_{i,I}^{j}), \tag{3.6}$$

where N_{arc} is the total number of measurements in an arc of lock (the path of the satellite viewed by the receiver in an epoch). Using Equations 3.5a and 3.5b into 3.6, one gets

$$W = \frac{1}{N_{arc}} \sum_{n=1}^{N_{arc}} [c(DCB^j + DCB_i) - c(DPB^j + DPB_i) - n_i^j]. \tag{3.7}$$

As in this work we interpret DCB_i, DCB^j, DPB_i, DPB^j to be constants at least in an arc; and also, if there are no cycle slips in phase ($n_i^j = constant$), 3.7 can be rearranged as

$$-c(DPB^j + DPB_i) - n_i^j = W - c(DCB^j + DCB_i), \tag{3.8}$$

that is, as all of the terms in 3.8 are constants for each arc, the mean operator $1/N_{arc} \sum$ fades away[2].

[2]Actually, W is calculated in practice using directly the average of the values of the observable differences (Equation 3.6); the algebraic maneuver in Equations 3.7 and 3.8 was just for finding an equation as simple as possible like 3.9.

Finally, by isolating the $STEC$ in 3.5b and combining it with 3.8, we cancel out the ambiguity term and the differential phase biases; then the $STEC$ will be given by (THEMENS et al., 2013)

$$STEC_i^j = \frac{1}{40.3}\left(\frac{f_1^2 f_2^2}{f_1^2 - f_2^2}\right)(\Phi_{i,I}^j + W - cDCB_i - cDCB^j). \tag{3.9}$$

The differential code bias for satellites, DCB^j, are monthly available for downloading; they are calculated using the differences $P_1 - P_2$ and $P_1 - C/A$, often shared in ns. Therefore, to match our modelling on code $(P_2 - P_1)$, the downloaded DCB^j on $P_1 - P_2$ must be multiplied by minus one, and to convert it from ns unity to $TECU$ the following Equation was used:

$$DCB^s[TECU] = -\frac{1}{40.3}\left(\frac{L_1^2 L_2^2}{L_1^2 - L_2^2}\right)\frac{c}{10^{16}}\frac{DCB^s[\text{ns}]}{10^9} = -2.8539 DCB^s[\text{ns}],$$

where L_1 and L_2 are the GPS frequencies previously mentioned. In this research, we restrict ourselves to find receiver differential code biases on $P_1 - P_2$ for receivers able to store P_1 information, and on $C/A - P_2$ for receivers having just C/A data on L_1[3]. It means that the term DCB_i in 3.9 will follow the same logic as DCB^j to become in $TECU$; therefore, the terms of the receiver and satellite biases in 3.9 will become positive after setting such equation in $TECU$.

In this work, we restrict the TEC analysis to satellites with elevation angle ϵ greater than 30° in order to avoid multipath effects and large errors due to mapping function. Such function, also known as slant factor, is derived from the single layer ionosphere model (SLIM) and it is given by

$$s(\epsilon) = \cos\chi = \cos\left(\arcsin\left(\frac{R_E \cos\epsilon}{R_E + h}\right)\right), \tag{3.10}$$

where χ is the zenith angle in the intersection of the satellite signal path with the *Ionospheric Pierce Point* (IPP), R_E is the main radius of the Earth, h is the height of the ionosphere, here assumed to be 400 km; the choice of the fixed ionospheric height will be justified in the next Chapter. The function 3.10 is represented in Figure 3.5 for an ionospheric height fixed at 400 km.

Figure 3.6 shows the elevation and azimuth angle for all GPS satellites in sight of

[3]The satellite bias on $C/A - P_2$ is obtained by the difference of the bias on $(P_1 - P_2)$ and $(P_1 - C/A)$.

Figure 3.5 - Slant factor.

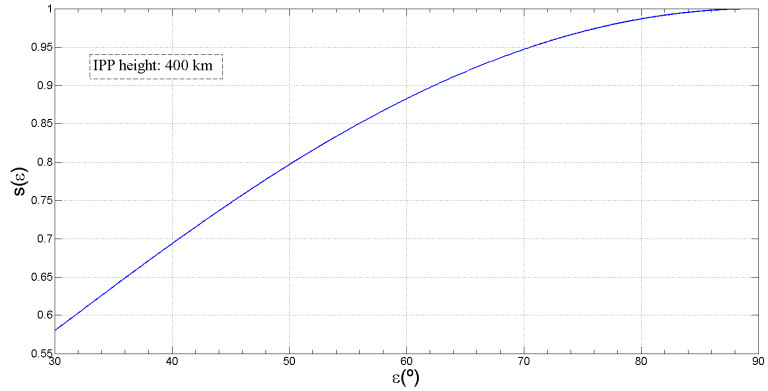

Slant factor as a function of the satellite elevation angle for an ionospheric height fixed at 400 km.

SOURCE: The author.

Fortaleza station in Brazil on March 21, 2021. Notice that only orbits with elevation greater than 30° degrees are shown by the figure.

The computation of the absolute $STEC$[4], the cycle slip repairs, the satellite azimuths and elevations, and the coordinates of the IPPs were performed by the *University of Texas at Dallas* code for TEC calibration.

Using Equation 3.10, we can rewrite 3.9 in a compact way as (MA; MARUYAMA, 2003)

$$VTEC = (STEC - B^s - B_r)s(\epsilon), \tag{3.11}$$

where $VTEC$ is the projection of the $STEC$ over the *Ionospheric Pierce Point* (IPP) schematically shown in Figure 3.7, B^s and B_r are, respectively, the satellite and receiver differential code biases with appropriate unities.

3.2 The ionosonde

The ionosonde is the equipment able to generate vertical plasma frequency profiles of the ionosphere. The ionosondes used in this work are of DIGISONDE type and the data were offered by the *DIvision of Heliophysics, Planetary sciences and Aeronomy* (DIHPA) and the *Division of Space Weather*, both at INPE. Basically, an ionosonde

[4]The slant TEC without any correction.

Figure 3.6 - Sky Plot.

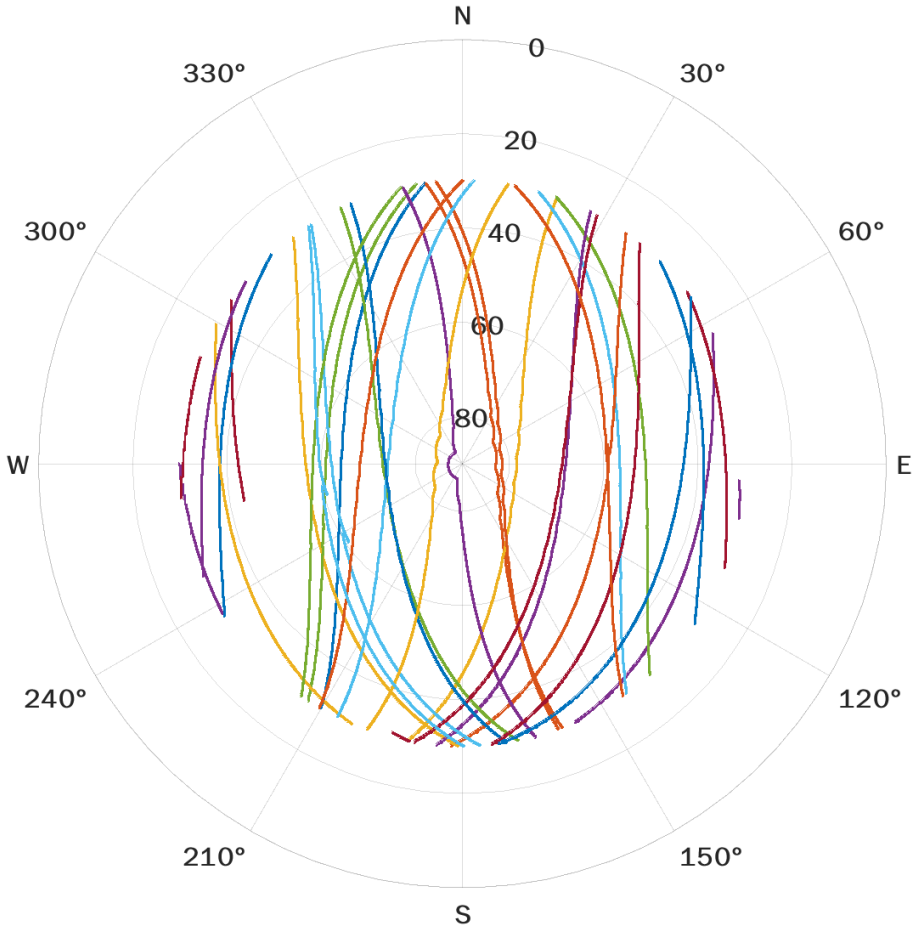

GPS satellite sky plot for the Fortaleza station in Brazil on March 21, 2021 for whole 24 hours. The radial coordinate is for the elevation angle and the angular parameter means the azimuth coordinate of the satellite in respect to the GNSS antenna.

SOURCE: The author.

is composed of a pulse transmitter and an arrangement of antennas, which by sweeping from frequencies between 0.5 and 30 MHz, measures the time elapsed between the transmitted pulse and the received echoes. Then, a vertical ionospheric profile up to the height h_mF_2 is generated, i.e, up to reach the maximum ionospheric plasma frequency f_mF_2. Such a profile is called *ionogram*, which represents the frequency in function of the virtual height. The ionospheric plasma density is derived from the simple formula

$$N_e = \frac{4\pi^2\epsilon_0 m_e}{e^2} f^2, \tag{3.12}$$

Figure 3.7 - Vertical TEC.

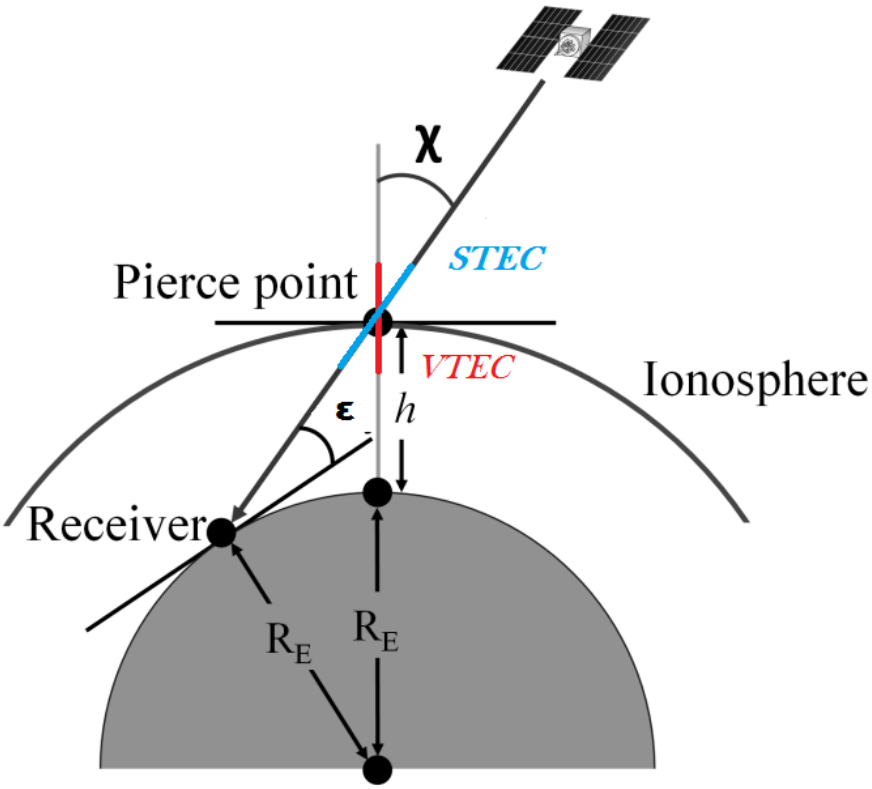

Conversion model of $STEC$ to $VTEC$ using SLIM model.
SOURCE: Adapted from Hein et al. (2016).

where ϵ_0, m_e, e and f are, respectively, the permittivity of the free space, the electron mass, the elementary charge and the signal frequency at which the wave is reflected.

The ionogram is plotted using the following equation

$$T = \frac{2h'}{c}, \tag{3.13}$$

being T the elapsed time and h' the virtual height, that is, the altitude at which an electromagnetic wave would be reflected if there were not free charges between the equipment and the reflection location, taking into account T. Actually, the waves have traveled at group velocity ($v_{gr} < c$), overestimating the virtual height in comparison with the real (or actual) height h. To understand how the $h' \rightarrow h$ conversion

can be performed, note that Equation 3.13 can be written as (SCOTTO et al., 2012)

$$h' = \int_0^T \frac{c}{2} dt, \tag{3.14}$$

and the group velocity is related to the velocity of light as $v_{gr} = c/n_{gr}$ (Equation 2.7a), where n_{gr} is the group refractive index. Also, n_{gr} is related to n_{ph} (known as phase refractive index) by

$$n_{gr} = n_{ph} + f\frac{d}{df}(n_{ph}). \tag{3.15}$$

Equation 3.15 provides $n_{gr} = 1/n_{ph}$, where n_{ph} is given in Equation 2.6. By substituting the relation between c and v_{gr} into 3.14 and taking into account that $v_{gr} = dh/dt$, this Equation becomes (SCOTTO et al., 2012)

$$h' = \int_0^h n_{gr} dh, \tag{3.16}$$

where,

$$n_{gr}^2 = \frac{1}{1 - \frac{\omega_N(h)^2}{\omega^2}}; \tag{3.17}$$

the terms $\omega_N(h)$ and ω in 3.17 are respectively the angular plasma frequency at h and angular wave frequency. The inversion of the integral Equation 3.16 provides the real height h. The analysis of 3.16 was performed through the *Standard Archive Output Format* (SAO-Explorer) software.

The topside of the profile is modeled using a Chapman function like 2.4. Figure 3.8 shows the ionospheric plasma frequency profile in MHz generated by ionosonde data from Cachoeira Paulista station in Brazil on March 21, 2021, at 6.5 LT. The topside model was derived from a Chapman function similar to 2.4.

3.3 Existing methods for receiver bias removal

In this section, we intend to illustrate two of the various methods for differential code bias removal in order to introduce our work and justify it. If an incorrect receiver bias is estimated, the corresponding $VTEC$ will be in error (RIDEOUT; COSTER, 2006).

Figure 3.8 - Electron plasma frequency from ionosonde.

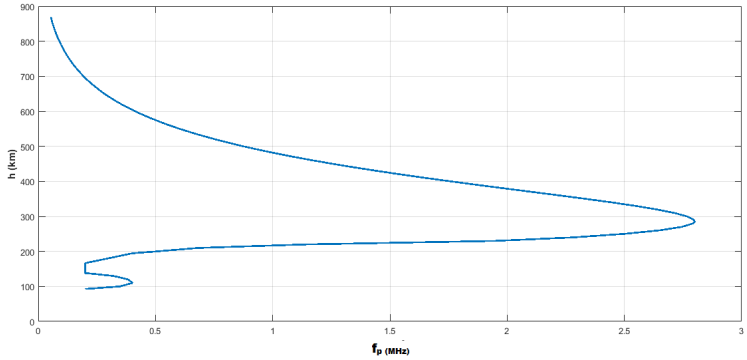

Vertical plasma frequency (MHz) profile generated by ionosonde data from Cachoeira Paulista station in Brazil on March 21, 2021, at 6.5 LT. The topside model was derived from a Chapman function.

SOURCE: The author.

Figure 3.9 shows an example of the $VTEC$ behavior with an estimated receiver bias lower than the right value, top panel; correct value, middle panel, and higher value, bottom panel. Additionally, according to the top panel of Figure 3.9, one can notice that the diverging $VTEC$ from the calculations of the satellites are mostly manifested in the beginning and in the end of the arc of observations. That is because the $VTEC$ given by Equation 3.11 has a proportional dependence on the slant factor (Equation 3.10 and Figure 3.5); that is, for a period of an approximately spatially uniform ionosphere, if the difference $STEC - B^s - B_r$ in 3.11 for various satellites are taken using wrong biases, the errors will grow proportionally to $s(\epsilon)$ as ϵ varies. Therefore, this Section is dedicated to discussing the task of correct bias removal and by discussing the scalloping method (CARRANO; GROVES, 2006) and the CADI-derived $STEC$ (THEMENS et al., 2013).

3.3.1 The scalloping method

In this method, it is assumed that the $STEC$ is a function of elevation while the receiver bias is not (CARRANO; GROVES, 2006). Therefore, in absence of spatio-temporal gradients, the $VTEC$ for various PRNs (Satellites) should be the same. Carrano and Groves (2006) used the time interval between 3 and 6 LT to compute

Figure 3.9 - $VTEC$ with incorrect and correct receiver bias removed.

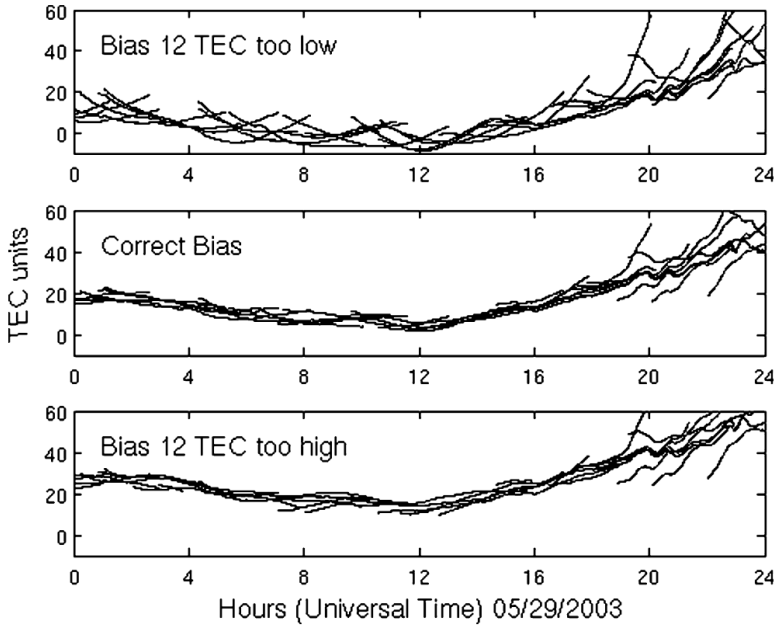

Example of the $VTEC$ behavior with an estimated receiver bias lower than the right value, top panel; correct value, middle panel, and higher value, bottom panel.

SOURCE: Rideout and Coster (2006).

the total variance, $V(B_r)$, of the calculated $VTEC$ given by

$$V(B_r) = \sum Var[VTEC(B_r)]_i, \tag{3.18}$$

where $Var[]_i$ notation indicated the i^{th} variance in a 12 minutes bin inside the window time interval 3-6 LT, and $VTEC$ is given in Equation 3.11, with B_s previously removed. The value which minimizes 3.18 is taken as the receiver bias. Figure 3.10 illustrates the procedure applied at Cuiabá station, Brazil on October 15, 2005. The best estimative for B_r was 22.3 $TECU$.

3.3.2 Receiver bias removal using CADI-derived STEC

Some assumptions used in the last method, for example, no spatio-temporal gradients may not be maintained at high latitudes. Thus, Themens et al. (2013) proposed the application of a bias removal method using *Canadian Advanced Digital Ionosonde* (CADI) measurements. The idea is simple; a set of GPS $STEC$ and CADI TEC are collected simultaneously, succeeded by the mapping of CADI TEC to be

Figure 3.10 - Receiver bias via scalloping method.

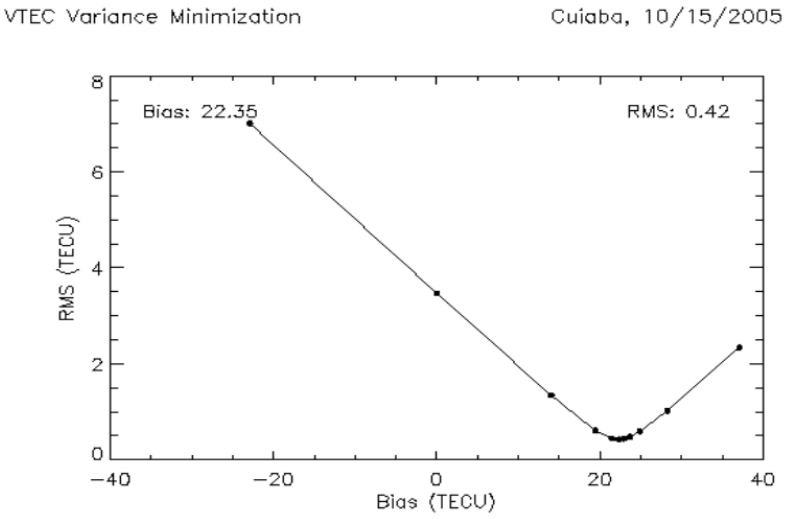

Total variance of $VTEC$ as function of B_r for Cuiabá station in Brazil on October 15, 2005. The best estimative for B_r was 22.3 $TECU$.

SOURCE: Carrano and Groves (2006).

equivalent to $STEC$ and subsequently, a linear regression is performed between the CADI-derived $STEC$ and GPS $STEC$. The y-intercept is taken as the receiver bias, considering that B_s was appropriately removed before the regression calculations. Figure 3.11 shows such analysis using data from Resolute Bay station for September 16-24, 2009. The bias was found to be 33.27 $TECU$.

Our method is somewhat similar to that presented by Themens et al. (2013) and we will describe it in the next section.

3.4 Receiver bias removal using ionosonde-derived TEC

The method proposed in this work intends to use ionosonde data from Brazilian sector to calibrate GPS TEC. Furthermore, considering that the significant space variation in the South American ionosphere occurs in magnetic latitude in the early hours of the day, we extended the method from the punctual coordinates, where ionosondes are operating, to a fitted function on magnetic latitude to make the approach applicable over whole Brazilian sector and some neighborhoods.

The method, basically, consists in choosing a local time for a set of ionosonde sta-

Figure 3.11 - Receiver bias via CADI.

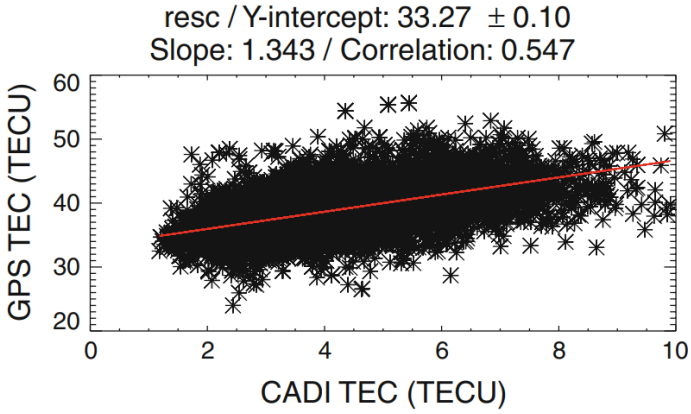

CADI $STEC$ versus GPS $STEC$ data from Resolute Bay station for September 16-24, 2009. The bias was found to be $B_r = 33.27\ TECU$.

SOURCE: Themens et al. (2013).

tions when the ionosphere is supposed to vary slightly in time and with minimal longitudinal gradients to calculate $IONTEC$ (TEC derived from ionosonde data) using the adapted α-Chapman function for the topside model; and, use the obtained $IONTEC$ data set to adjust a curve and calibrate the GPS TEC data derived from a specific receiver.

3.4.1 Ionosonde-derived TEC (IONTEC)

After choosing a reference time, t, the ionogram for t is edited and important parameters are extracted. The virtual height is converted into real height and the vertical frequency profile is converted into electron density using Equation 3.12. After these processes, we are left with the vertical electron density profile up to h_mF_2 where the density peak is $N_{e,m}F_2$. The next step consists in modeling the topside. Here, we used the adapted α-Chapman function (JAKOWSKI, 2005) in order to include the plasmasphere, for the satellites orbiting about 20,000 km. The model is given by (KLIPP et al., 2020)

$$N_T(h) = N_{e,m}F_2 \exp\left(\frac{1}{2}(1 - z - e^{-z})\right) + N_0 \exp\left(\frac{-h}{H_P}\right), \tag{3.19}$$

where $z = (h - h_mF_2)/H_T$ is the reduced height for the ionosphere. The parameters H_T (F_2 scale height), h_mF_2 and $N_{e,m}F_2$ are derived from ionograms. The

plasmaspheric scale height, H_P, is defined as 10,000 km (JAKOWSKI, 2005) and $N_0 = k \cdot N_{e,m}F_2$, with $k = 1/175$ empirically determined by Klipp et al. (2020) for the Brazilian sector. Finally, the bottom ionosphere profile derived from ionosonde, $N_B(h)$, is integrated and summed with the integration of $N_T(h)$ to give rise to $IONTEC$, where the last integral is performed from h_mF_2 until 20,000 km; that is,

$$IONTEC = \int_0^{h_mF_2} N_B(h)dh + \int_{h_mF_2}^{20{,}000\text{ km}} N_T(h)dh. \tag{3.20}$$

Figure 3.12 is an illustration of the terms in Equation 3.20, being the black and red profiles for $N_B(h)$ and $N_T(h)$, respectively; and, the two distinct gray areas are for the two integral in 3.20.

Figure 3.12 - Obtaining the $IONTEC$.

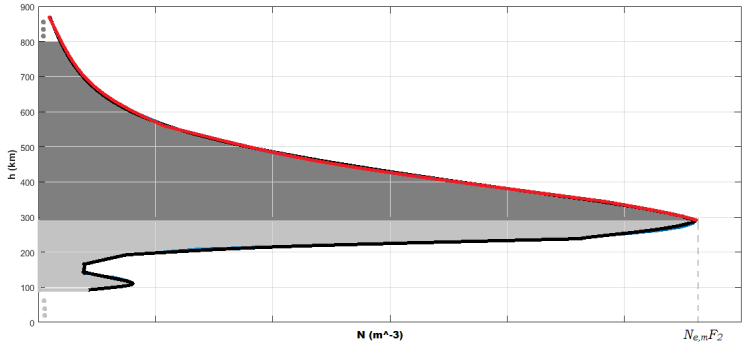

Illustration of the terms in Equation 3.20. The black and red profiles for $N_B(h)$ and $N_T(h)$, respectively; and, the two distinct gray areas are for the two integral in 3.20.

SOURCE: The author.

Assuming that the ionosphere does not have significant TEC gradients on its magnetic longitudinal distribution at t=6.5 LT, it is possible to collect a set of $IONTEC$ data from the Brazilian ionosondes operating and fit a function on their magnetic latitudes, $IONTEC(M_{lat})$. Table 3.1 shows the six ionosonde stations operating in Brazil from the 21^{st} to 23^{rd} of March 2021, as such as their code, geographic coordinates, and magnetic latitude. For those stations, we performed 3.20 and fitted a

polynomial function of degree 2[5],

$$IONTEC(M_{lat})[TECU] = a_2 M_{lat}^2 + a_1 M_{lat} + a_0, \tag{3.21}$$

being M_{lat} the magnetic latitude, the coefficients a_is for the 6.5 LT of the three days are shown in Table 3.2 and their functions are shown in Figure 3.13, where the red circles and line are the data and fitted function for March 21, respectively; the green circles and line are the same for March 22; and, the blue circles and line are for the day 23. In the following subsection, we explain how we have used 3.21 to extract the DCB from the Brazilian GNSS receivers.

Table 3.1 - List of Digisonde stations used in this study.

Station	Code	GLat.	GLon.	MLat.
Boa Vista	BVJ03	2.845°N	60.701°W	8.693°N
São Luís	SAA0K	2.593°S	44.212°W	4.864°S
Fortaleza	FZA0M	3.877°S	38.425°W	9.346°S
Campo Grande	CGK21	20.466°S	54.662°W	14.691°S
Cachoeira Paulista	CAJ2M	22.687°S	44.985°W	21.656°S
Santa Maria	SMK29	29.719°S	53.716°W	21.983°S

Table 3.2 - $IONTEC$ function Coefficients for 6.5 LT of March 21, 22, and 23, 2021.

day\Coeff.	a_2	a_1	a_0
21	-0.0036	-0.04407	6.91448
22	-0.00951	-0.09973	7.33796
23	-0.01224	-0.1342	7.57094

3.4.2 GPS-derived TEC calibration using IONTEC

Each satellite from the GPS constellation is labeled according to its *PseudoRandom Noise code* (PRN) and their DCB can be downloaded at `ftp://ftp.unibe.ch/aiub/CODE/`. Currently, 32 PRNs are operating and we will refer to each one by its PRN series in the constellation, for example, the satellite number 25 of the GPS constellation will be named PRN 25. To calibrate the data of all PRNs in sight, we

[5]It is worth mentioning that for the period of analysis, the solar activity was low and it aids the choice of an simple polynomial fitting of degree 2. Such assumption may not hold for high solar activity periods and a higher degree might be necessary.

Figure 3.13 - Magnetic latitude versus $IONTEC$.

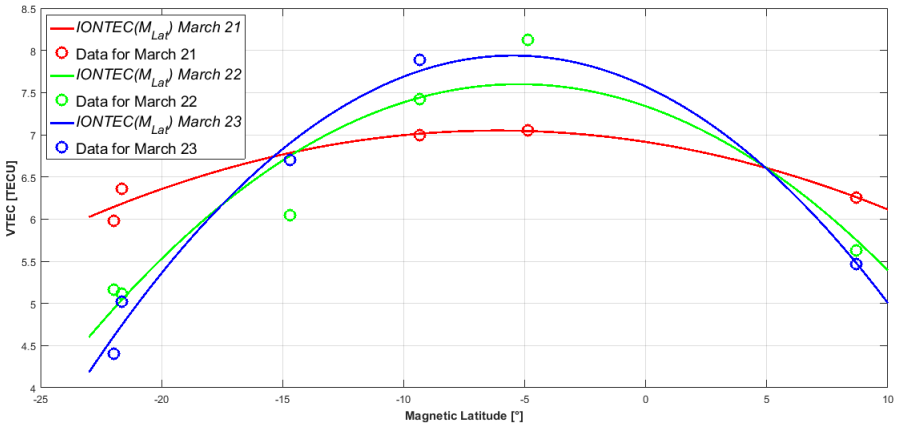

Ionosonde data and fitted functions 3.21 for 6.5 LT of March 21, 22, and 23, 2021. The red circles and line are the data and fitted function for March 21, respectively; the green circles and line are the same for March 22; and, the blue circles and line are for the day 23.

SOURCE: The author.

use the Equation 3.11 for a fixed receiver r,

$$VTEC_r^s(t) = (STEC_r^s(t) - B^s - B_r)s(\epsilon_r^s(t)), \tag{3.22}$$

where t, and s=1,2,. . . ,32 are for time and a specific PRN, respectively. As the satellite DCB is known for each satellite as such as the set of uncalibrated $STEC_r^s(t)$, a good measurement of $VTEC_r^s(t)$ for a specific time would make Equation 3.22 to be a simple equation on B_r; for this, we take the $IONTEC(M_{lat})$ as $VTEC$; also, we tag the receivers by their magnetic latitudes and use the measurements of $STEC_r^s(t)$ made at t=6.5 LT to match the fitted function. Thus, the DCB of a receiver with magnetic latitude M_{lat} will be given by

$$B_r = B_r(M_{lat}) = STEC_r^s(6.5) - \frac{IONTEC(M_{lat})}{s(\epsilon_r^s(6.5))} - B^s. \tag{3.23}$$

As we are considering various PRNs seen by a receiver at t, we are left with a vector $\mathbf{B}_r$, where its number of elements is equal to the number of PRNs in sight; the $\mathbf{B}_r$ components may differ due to several unmodeled factors. To minimize this, we take B_r as the average of the vector of estimated biases, $< \mathbf{B}_r >$. After this process, the

Equation 3.22 is used to calibrate the $VTEC$.

3.4.3 Outlier removal

Whenever we are working with data, certain care must be taken. Several factors might give rise to data which are behaving differently from the overall trend. Such data points are often termed outliers. Outliers can occur in data collecting due to unknown phenomena, human and/or instrumental errors in the data management. In this work, without further discussions, we assume that these data do not contain significant information and can be detected and discarded. For this, we implement the *Z-score* treatment. Also, we assume that the unmodeled factors acting on our system normally distribute our estimations about the mean value of $\mathbf{B}_r$. Therefore, the Z-score for the i^{th} sample, B_{r_i}, is given by

$$z_i = \frac{B_{r_i} - < \mathbf{B}_r >}{\sigma_{\mathbf{B}_r}}, \tag{3.24}$$

where $\sigma_{\mathbf{B}_r}$ is the standard deviation of $\mathbf{B}_r$. We establish 1 as the threshold at which values of $|z_i|$ higher than this, imply discarding B_{r_i}. Table 3.3 shows the approach applied once for the Brazilian station Coari on March 21, 2021, wherein the first column we have the PRN code of the satellites used in this calculation, the second column shows their elevation angles at 6.5 LT, the calculation of the bias determined through each PRN using 3.21 and 3.23 are shown in the third column, and the fourth column exhibits the Z-score of each estimation. Obviously, the bias calculation performed using the PRN 10 was discarded. After this, the actual receiver bias is taken as the average of the remaining components, that is, the mean value of the components of $\mathbf{B}_r$ that have Z-score between -1 and 1.

Table 3.3 - Z-score for outlier removal applied on Coari station for its bias calculation.

PRN	$\epsilon[^\circ]$	$B_{r_i}[TECU]$	z_i
10	64.0670	-100.3477	-1.4375
20	63.8960	-94.4010	0.9290
23	70.3380	-95.0066	0.6880
25	45.9863	-95.6063	0.4493
26	41.6398	-98.3152	-0.6287

3.5 TEC map generation

Once calibrated the GNSS-derived TEC data, we are left with a set of k data, $TEC(t)_i$ with $i = 1, .., k$, at an instant t with latitude $\varphi(t)_i$ and longitude $\lambda(t)_i$; the coordinates depend on t because they represent the location of the IPP referent to each pair satellite-receiver, which vary in time due to the orbital motion of the satellites. However, for better visualization of some geospatial physical behavior, it is worth using some reasonable technique to extend the coverage of the information from punctual data observations to regional maps of the specific phenomenon.

Parker (1994) and Wessel and Becker (2008) applied interpolation on the unit sphere for geomagnetic analyzes whereas Mendoza et al. (2020) and Oliveira et al. (2020) applied similar procedures for TEC gridding. In this research, we generated the TEC maps using interpolation with *the minimum curvature solution* (PARKER, 1994). According to Wessel and Becker (2008), the main advantages of using such an approach are (1) the simplicity of implementation, (2) the capability of using surface gradients as constraints, and (3) the freedom to use any configuration of input and output coordinates, not necessarily uniformly spaced. The method presented by Parker (1994) searches for a function f, such that,

$$d_i = f(\hat{\mathbf{r}}(\varphi_i, \lambda_i)) = f(\hat{\mathbf{r}}_i), \tag{3.25}$$

where $\hat{\mathbf{r}}(\varphi_i, \lambda_i)$ is the unitary vector mapping the data coordinates on the unitary spherical surface, S^2, and d_i, $(i = 1, ..., k)$, is the set of observed (or measured) data; to guarantee the smoothness of f, the following integral must be minimized (PARKER, 1994; WESSEL; BECKER, 2008)

$$\int_{S^2} (\nabla_S^2 f)^2 d^2\hat{\mathbf{r}}. \tag{3.26}$$

As the interpolation is deduced on the unitary sphere, the Laplacian operator in 3.26 reduces as

$$\nabla_S^2 = \frac{1}{r^2}\frac{\partial}{\partial r}\left(r^2\frac{\partial}{\partial r}\right) + \frac{1}{r^2\sin\theta}\frac{\partial}{\partial\theta}\left(\sin\theta\frac{\partial}{\partial\theta}\right) + \frac{1}{r^2\sin^2\theta}\frac{\partial^2}{\partial\lambda^2} \tag{3.27a}$$

$$= \frac{\partial^2}{\partial\theta^2} + \cot\theta\frac{\partial}{\partial\theta} + \frac{1}{\sin^2\theta}\frac{\partial^2}{\partial\lambda^2}, \tag{3.27b}$$

where θ is the colatitude. An advantageous approach is to expand f in *spherical harmonics* (SH), $Y_l^m(\theta, \lambda)$ (degree l and order m), owing to the fact that they are eigenfunctions of ∇_s^2,

$$\nabla_s^2 Y_l^m = -l(l+1)Y_l^m. \tag{3.28}$$

Parker (1994) analyzed the case by SH and Wessel and Becker (2008) used *generalized Green's function*, g, for the surface Laplacian operator, where both found a solution in the form

$$f(\hat{\mathbf{r}}) = \frac{\beta}{2\sqrt{\pi}} + \sum_{i=1}^{k} \alpha_i g(\hat{\mathbf{r}}, \hat{\mathbf{r}}_i), \tag{3.29}$$

where β is an arbitrary constant, α_i are coefficients to determine and writing γ as the angle between $\hat{\mathbf{r}}$ and $\hat{\mathbf{r}}_i$ (WESSEL; BECKER, 2008),

$$g(\gamma) = -\frac{1}{4\pi}\mathrm{dilog}\left(\sin^2\frac{\gamma}{2}\right), \tag{3.30}$$

being $\mathrm{dilog}(x)$ the dilogarithm function given by the following integral equation (ABRAMOWITZ et al., 1988)

$$\mathrm{dilog}(x) = -\int_1^x \frac{\ln u}{u-1} du. \tag{3.31}$$

We proceed in the map generation similar to Wessel and Becker (2008), setting $\beta = 2\sqrt{\pi} < TEC_i >$ in a such way that Equation 3.29 becomes

$$TEC(\hat{\mathbf{r}}) =< TEC_i > + \sum_{i=1}^{k} \alpha_i g(\hat{\mathbf{r}}, \hat{\mathbf{r}}_i); \tag{3.32}$$

also, the vector $\Delta TEC_i = TEC_i - < TEC_i >$ is used to constrain the coefficients α_i ($[\alpha_i]$=$TECU$) by solving the squared linear system (MENDOZA et al., 2020; WESSEL; BECKER, 2008)

$$\Delta TEC_h = \sum_{i=1}^{k} \alpha_i g(\hat{\mathbf{r}}_h, \hat{\mathbf{r}}_i). \tag{3.33}$$

We can summarize the map generation procedure as follows: (1) obtaining the calibrated TEC data by means of the methods described in the previous section; (2) averaging the data in cells of 1°×1° over the South American sector similar to Mendoza et al. (2020) in order to reduce the noise in the data; (3) finally, 3.32 and 3.33 are evaluated by the MATLAB code provided by Dr. Wessel (Wessel and Becker (2008)).

Mendoza et al. (2020) performed the averaging in cells with resolution 0.5°×0.5°,

due to their better coverage of the South American GNSS stations and the implementation of various constellations, and cells with few observations were discarded. Also, the $TEC(\hat{\mathbf{r}})$ from Mendoza et al. (2020) uses the method derived by Wessel and Becker (2008), where a parameter called *tension* is introduced in the deductions of the generalized Green's function in order to prevent the interpolated function to oscillate far from the data constrains. The TEC maps of Mendoza et al. (2020) are available at `https://www.maggia.unlp.edu.ar/articulo/2017/1/6/monitoreo_ionosfera` as products of the *Laboratorio de Meteorología Espacial, Atmósfera Terrestre, Geodesia, Geodinámica, diseño de Instrumental y Astrometría* (MAGGIA laboratory). Figure 3.14 shows an example of a TEC map with IONEX[6] data from the MAGGIA laboratory. From now on, we will refer to those maps as MAGGIA maps. Also, the wide coverage of the MAGGIA map is owing to the fact that the laboratory uses data from GNSS stations in Central America and in some islands of the Atlantic Ocean, making it possible to extrapolate the map for the southern parts of the North America and the western region of the African continent.

Figure 3.15 shows the three main steps for the TEC map generation previously described for March 21, 2021, 1 UT, using data from the RBMC network; in the three sub Figures, the red line represents the magnetic equator, whereas in the left side panel (3.15a) it is shown the calibrated TEC ($VTEC$) data by the adjusted $IONTEC$ function; the central panel (3.15b) shows the TEC average per cell, each one with resolution $1°\times1°$; and, 3.15c exhibits the final result, $TEC(\hat{\mathbf{r}})$ evaluated in a grid with resolution $0.5°\times0.5°$. Of course, the interpolated function generated by 3.32 and 3.33 would be extended and evaluated over the whole globe. However, it should not reflect the TEC behavior in a reasonable way far from the data coordinates. Therefore, we constrain $TEC(\hat{\mathbf{r}})$ to be evaluated solely in coordinates such that their positions are less than $4°$ of angular distance from the closest IPP. Also, unlike Mendoza et al. (2020), we do not discard the averaged cells with few observations in order to investigate the small structures in the ionosphere.

[6] (*IONosphere map EXchange*) (SCHAER et al., 1998).

Figure 3.14 - MAGGIA *TEC* map.

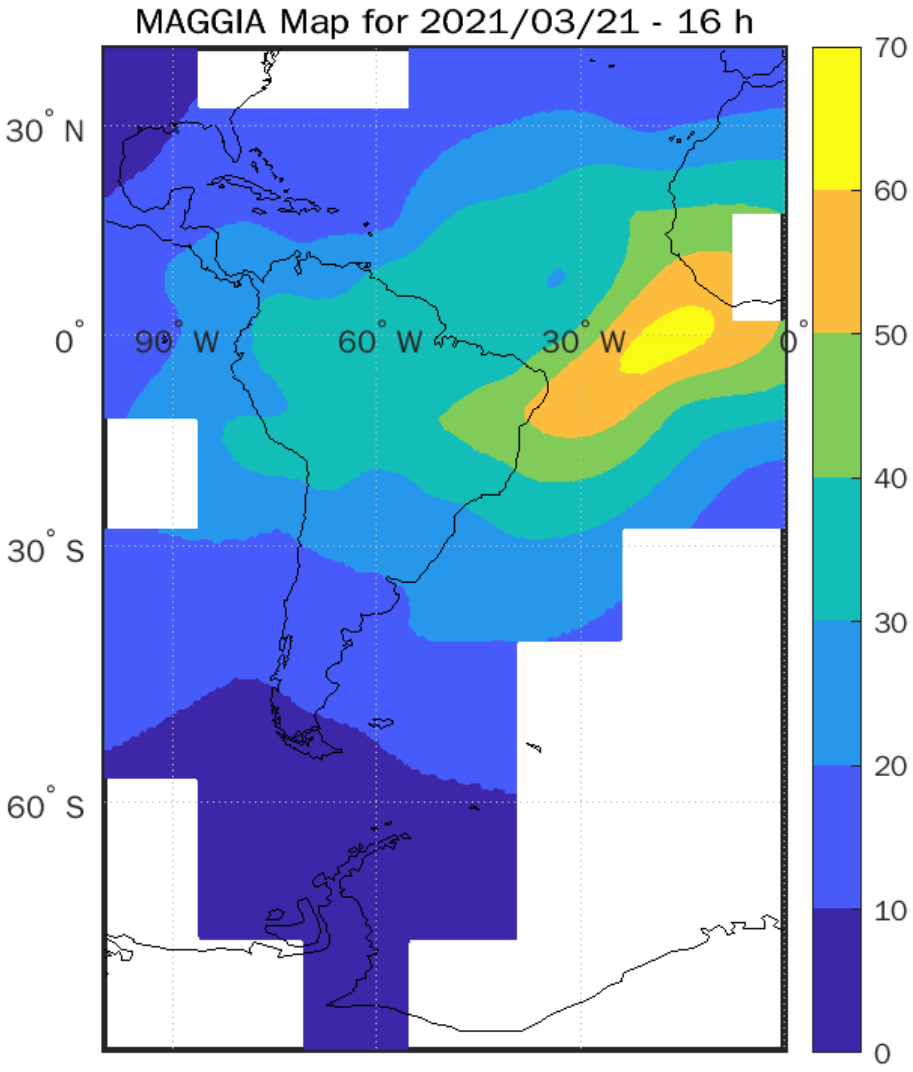

TEC map made with data from MAGGIA laboratory for March 21, 2021, 16 UT. The color bar is in *TECU*.

SOURCE: The author.

Figure 3.15 - TEC map generation steps.

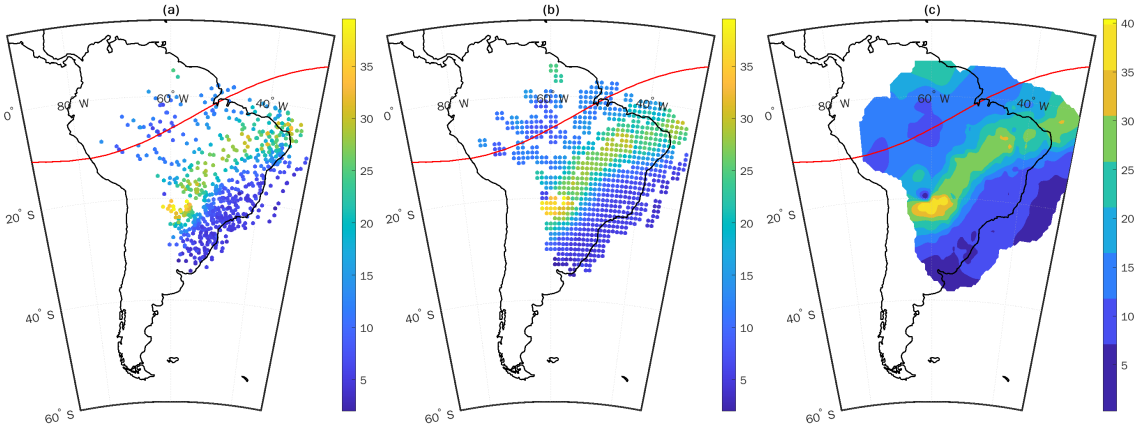

a b c

Three main steeps of the TEC map generation for March 21, 2021, 1 UT. The red line represents the magnetic equator; the left panel (a) shows the distribution of the calibrated TEC data, at the center, the averaged data within cells of 1°×1°, and the right panel (c) shows the $TEC(\hat{\mathbf{r}})$ evaluated on cells of 0.5°×0.5° of resolution closer to the data coordinates. All of the three color bars are in $TECU$.

SOURCE: The author.

4 RESULTS AND DISCUSSIONS

As mentioned before, we have performed the method described in the last section of Chapter 3 for March 21, 22, and 23, 2021 using ionosonde data from six stations as listed in Table 3.1, with local time used for $IONTEC$ calculation t=6.5. The TEC data were obtained from RINEX files in 15 seconds of time resolution, downloaded from Instituto Brasileiro de Geografia e Estatística (IBGE) (2021), whose stations compose the *Rede Brasileira de Monitoramento Contínuo dos sistemas GNSS* (RBMC); also, two more networks where attached in our analysis in order to improve the coverage of our maps, they are from the *Instituto Nacional de Ciência e Tecnologia – Tecnologia GNSS no Suporte à Navegação Aérea* (INCT GNSS-NavAer) (MONICO et al., 2022) and Système d'Observation du Niveau des Eaux Littorales (SONEL) (2022). The localization of each RBMC, INCT and SONEL networks receiver/station and the ionosondes (of DIGISONDE type) used for our calculations are shown in Figure 4.1. Notice that there is a large gap of ionosonde stations in Brazilian territory; this fact might become a problem to apply the method in periods of high solar activity.

In the previous chapter, we have assumed that the ionospheric height, h, for our purpose would be constant, fixed at 400 km. Its a reasonable assumption to simplify the calculations. To make sure that the choice of a constant h does not make significant influence on the bias calculations, we analysed what would happen to the results if we vary h. Figure 4.2 allows a quantitative analysis; where we have the bias estimation in the horizontal axis (in $TECU$) in function of the chosen ionospheric height, represented by the vertical axis in km. In Figure 4.2, the dashed lines show the influence of the arbitrary choice of h on the bias inference of three stations containing ionosonde devices and GNSS receivers, São Luís, Santa Maria, and Cachoeira Paulista; and, the solid lines are for two stations just owing GNSS antenna, Arapiraca and Coari, whose $VTEC$ was obtained using the fitted function $IONTEC(M_{lat})$. It is sufficient to show that whatever is the choice of h (Between 250 and 450 km), no substantial discrepancy will be introduced into the results.

Also, the method was compared with an already existing code for TEC calibration which uses the scalloping technique, previously discussed in Chapter 3. The code is the *University of Texas at Dallas* (UTD) code for TEC calibration (private communication with Cesar Valladares, 2022). Both methods are in good agreement as shown in the first results indicated in Figures 4.3 and 4.4.

As the data are shared in UT, due to differences between Brazilian LT and UT,

Figure 4.1 - Localization of the GNSS receivers from the networks RBMC, SONEL, INCT and Digisondes.

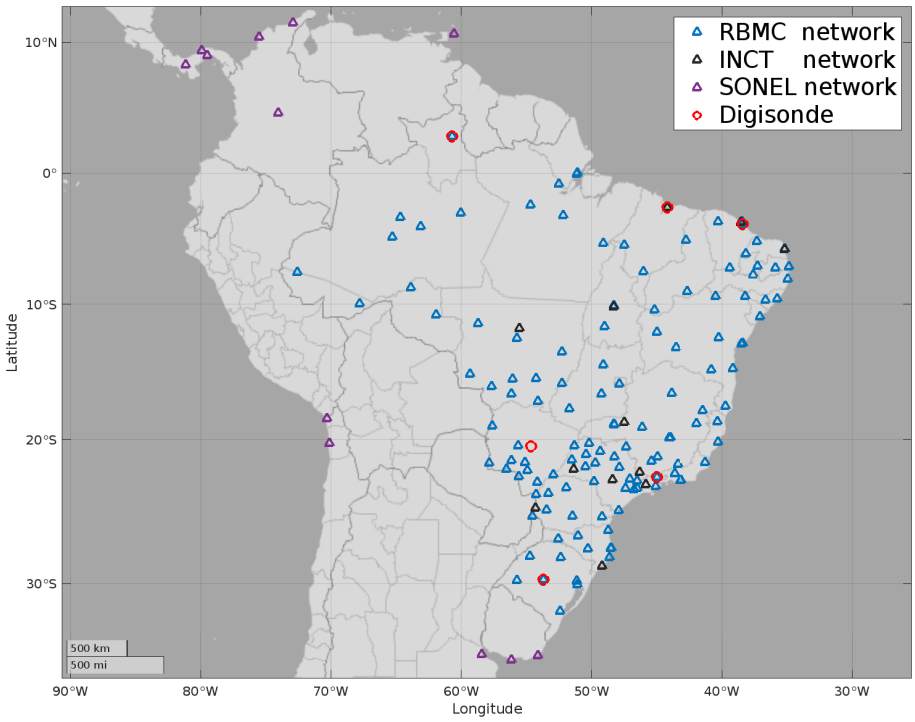

Positions of the RBMC stations (blue triangles), INCT stations (black triangles), SONEL stations (purple triangles) and the DIGISONDES (red circles).

SOURCE: The author.

the graphics also show the ionospheric behavior for the last hours of March 20, 2021 (negative values in the horizontal axes). Note, also, that the stations Boa Vista (4.3a), Fortaleza (4.3b) and São Luís (4.3c) observed strong scintillation before midnight LT. It is owing to the fact that they are in the north and northeast regions of Brazil (see Figure 4.1) susceptible to observe the *Equatorial Ionization Anomaly* (EIA) as seen in the map generated in Figure 3.15.

For Figures 4.3a, 4.3b, 4.3c, 4.4a, and 4.4b, the left panel shows the TEC calibrated with ionosonde data, while the right panel is for the TEC calibrated with UTD code. Also, the left panel of each station shows the receiver DCB value inferred via ionosonde data, the number of PRNs in such analysis, the time chosen for the calibration, the standard deviation of the bias measurement, and the minimum elevation used to approve a satellite data. In the right panel is shown the receiver DCB value inferred via UTD code, the name of the station, and its magnetic latitude.

Figure 4.2 - Influence of the chosen ionospheric height, h, on the bias estimations.

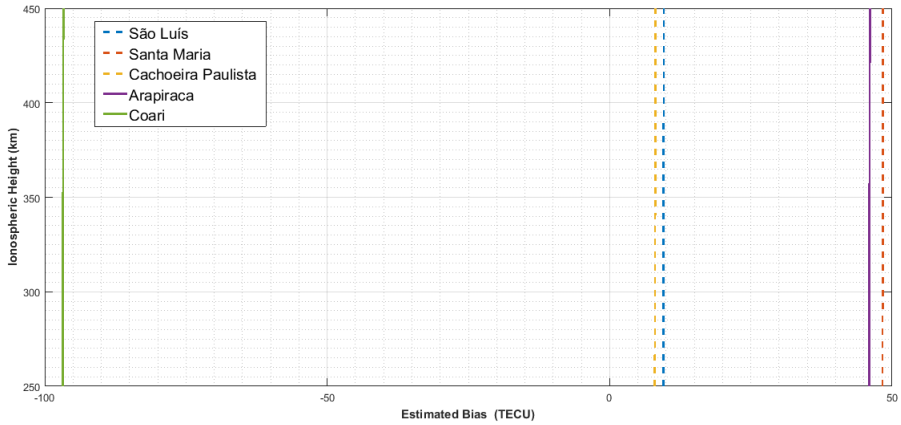

Bias estimation in the horizontal axis (in $TECU$) in function of the chosen ionospheric height, represented by the vertical axis in km. The dashed lines show the influence of the arbitrary chose of h on the bias inference for São Luís, Santa Maria, and Cachoeira Paulista stations. Whereas the solid lines are for Arapiraca and Coari.

SOURCE: The author.

In Figure 4.5, are shown the calibrated TEC for Arapiraca and Coari stations in the same way as in Figures 4.3 and 4.4; however, such stations do not have ionosondes operating simultaneously as the previously discussed stations. For those places, the TEC calibrations were entirely performed by the $IONTEC(M_{lat})$ function. For the Arapiraca station, Figure 4.5a, both methods found a very similar DCB, where $IONTEC$ method found a bias of 46.1113 $TECU$ and the UTD code inferred 47.00 $TECU$. However, Figure 4.5b deserves some discussions. Note that in the calculations made by the UTD code (right panel of 4.5b), a PRN seems to diverge from the others after 5 LT when it started to be observed by the station. This is the PRN 10, which was detected and removed in our calculations using the Z-score approach shown in Table 3.3. Also, one can notice that the TEC calibrated by the ionosonde data shows more uniform trends in the period of calm ionosphere, whereas the UTD plot shows a more irregular behavior similar to the example shown by Rideout and Coster (2006) in Figure 3.9, with incorrect biases estimation.

Receiver DCBs are usually expected to be approximately constant at least for a few days, supposing that the physical properties of the whole receiver parts (antenna, cable, plugs, or connections) do not change too quickly. To study the day-to-day

variability of the bias calculations was built the Figure 4.6, which represents the difference between the bias estimated in a specific day minus the bias estimated in the previous day for each receiver from the RBMC network. Note that a receiver has presented large variation (red line); it was the Cachoeira Paulista station and it will be discussed latter. Also, the black line in Figure 4.6 shows the average change from one day to the following one, for all of the receivers. Rideout and Coster (2006) found in their biases calculation a standard deviation of 2 $TECU$ for each receiver when analysing the day-to-day variability. By analysing Figure 4.6, even though some stations are showing variations greater than 2 $TECU$, the average standard deviation of the day-to-day bias variability was 0.6376 $TECU$.

Now, we turn back to the discussions about the Cachoeira Paulista station. Figure 4.7a shows the slant TEC (blue lines) for such station, the $F10.7$ and the Ap index during Mach 21, 22, and 23, 2021 whereas the horizontal red line is to show the zero point in the TEC scale. Note that a discontinuity occurs in the data of the second day during the transition time, i. e., at 0 and 24 UT. Figure 4.7b exhibits the TEC (also the blue lines) calibrated by our method for the same days showing the variation in the bias seen in Figure 4.6, in which the bias estimated for the first day was approximated 8 $TECU$, then, it decreases about 4 $TECU$ and consecutively increases to a value higher to the initial one. One explanation behind this is not a subject for this research right now, but a possible reason would be a less controlled environment for the station, which can provide daily variability on the receiver biases (WILSON; MANNUCCI, 1993). However, notice that whatever happened to this station during these days, our method was able to figure out and guarantee the continuity of the TEC data series, as seen in Figure 4.7b.

Figures 4.8a, 4.9a, and 4.10a show the TEC maps generated by the minimum curvature method, discussed in the last section of Chapter 3, at 1:17 UT for March 21, 2021; 2:30 UT for March 22, 2021; and 3:00 UT for March 23, 2021. Also the items b and c of the same figure show the All-Sky pictures from Instituto Nacional de Pesquisas Espaciais (INPE) (2021) and MAGGIA maps for equivalent time. The choice of these specific times follows the availability of All-Sky data. The All-Sky imager aid to identify plasma structures in the ionized atmosphere due to the airglow emission of the atomic oxygen in an atmospheric layer of approximately 150 km thick, centered about 250 km of altitude. In Figure 4.8b, is shown the data from the imager in São Jão do Cariri and it clearly exhibits dark structures, which are also seen in the Figure 4.8a. These shapes are plasma depletions (also called *Equatorial Plasma Bubbles* (EPBs)) signed by the lack of airglow emission in this

region similar to the ones noticed by Pimenta et al. (2003), where the authors described them as depletion bands quasi-north-south aligned. Such behavior is not shown in the MAGGIA map (Figure 4.8c), which shows a more smooth behavior of the ionosphere.

For the following day, March 22, 2021, at 2:30 UT, we have Figure 4.9 with the same characteristics as Figure 4.8. At this instant, one more imager was working in São Martinho da Serra and the three maps are not showing EPB signatures. However, the maps generated by our method (Figure 4.9a) and the MAGGIA map (Figure 4.9c) are showing differences in the ionospheric topology, where our map shows more defined EIA crests. A possible explanation to this behavior is the high level of smoothness applied by the MAGGIA method. Additionally, as said before, the MAGGIA method does not maintain cells with few samples in the process of spatial averaging of the calibrated TEC, where such data is used as input for the interpolation function calculation. As the coverage of our maps is more restricted, discarding cells will not be a compensatory choice in terms of computation; then, keeping the whole data set will provide more detailed ionospheric information, making the MAGGIA and $IONTEC$ maps to diverge in some cases.

Figure 4.10, also with the same structure of Figures 4.8 and 4.9, shows the analysis at 3:00 UT for March 23, 2021, where 4.10a is showing EPB signatures. The All-Sky data for this day and time is not clear enough to provide inference. Also, again the MAGGIA map (4.10c) is diverging in geometry from the one provided by our method, showing much more regular ionospheric behavior. However, Figure 4.10a shows interesting EPB features. The regions with low TEC values were also reported by Kil et al. (2004): distinct reverse C-shaped dark bands, which extend from the southern to the northern parts of the EIAs. Kil et al. (2004) found those structures in a period of the year similar to the used in this work, March 22-23, 2002. The MAGGIA method may did not detect these structures due to the sparse distribution of GNSS stations in the regions EPB occurrence together with the discarding cells process. To go further in the EPB analysis for those aforementioned days, we collected the *scintillation index* $S4$ from Instituto Nacional de Ciência e Tecnologia (INCT) (2022) and show them in Figure 4.11. Such Figure shows $S4 \geq 0.15$ from the satellites with elevation angles $\geq 20°$. Figures 4.11a (for March 21, 2021), 4.11b (for March 22, 2021), and 4.11c (for March 23, 2021) are coherent with the maps generated by our method shown in Figures 4.8a, 4.9a, and 4.10a, where the $S4$ index data for the first and last day in discussion corroborate the EPB occurrences; also, note that on March 22, no EPB signature was found in our map (4.9a), nor

significant scintillation levels (4.11b).

Figure 4.3 - TEC calibrated via ionosonde (left) and TEC calibrated via UTD for Stations of Boa Vista, Fortaleza and São Luís.

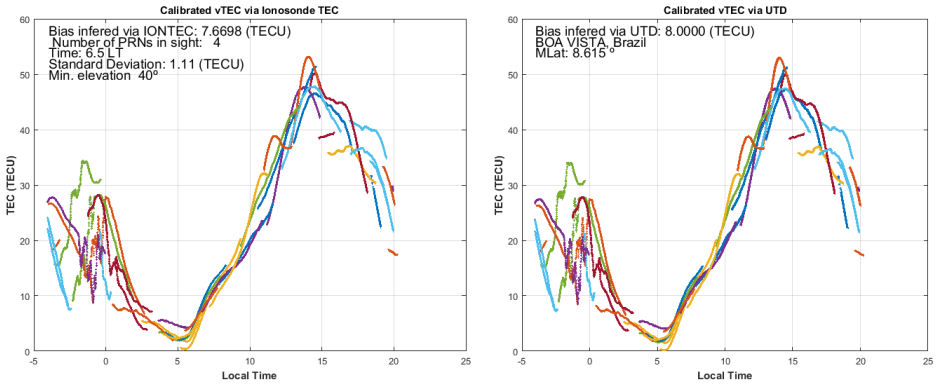

a

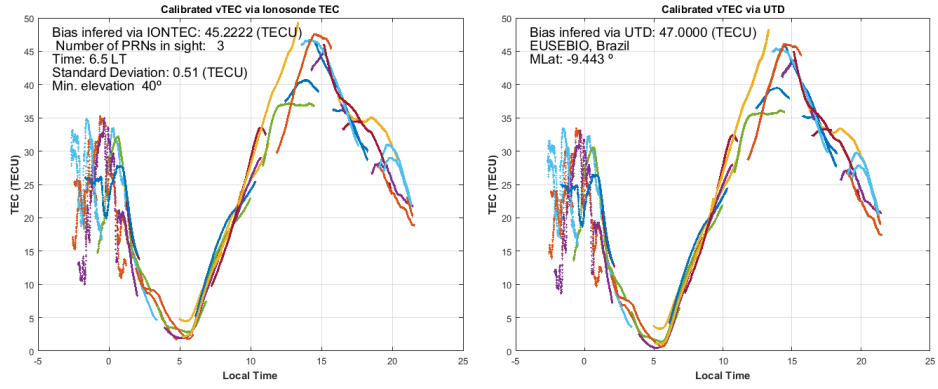

b

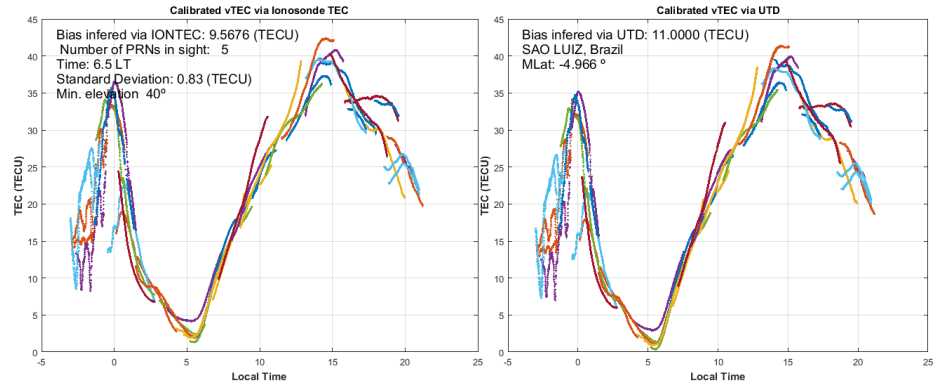

c

Comparison of the TEC calibration for Boa Vista in the top panel (a), Fortaleza in the middle panel (b), and São Luís in the bottom panel (c). For each station, the left plot shows the TEC calibrated via ionosonde data and the right one is for the calibration via UTD code.

SOURCE: The author.

Figure 4.4 - TEC calibrated via ionosonde (left) and TEC calibrated via UTD for Stations of Cachoeira Paulista and Santa Maria.

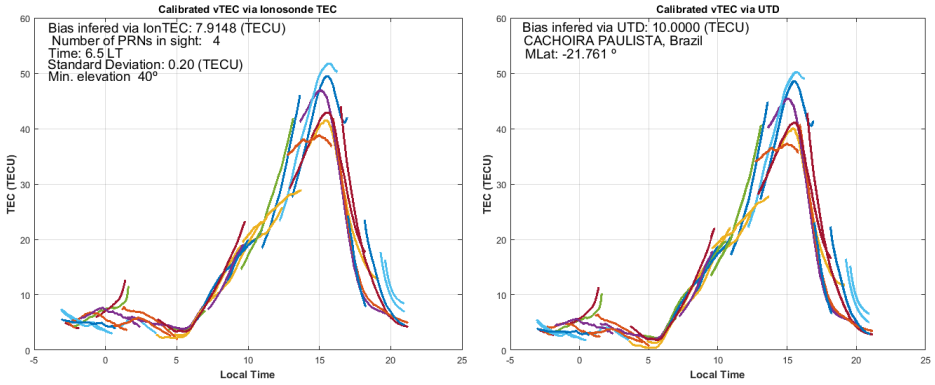

a

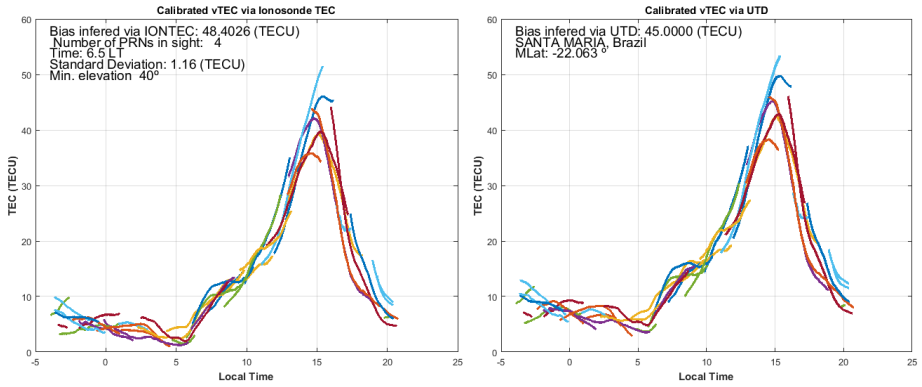

b

The same as Figure 4.3 for the stations of Cachoeira Paulista (a) and Santa Maria (b).

SOURCE: The author.

Figure 4.5 - TEC calibrated via ionosonde (left) and TEC calibrated via UTD for Stations of Arapiraca and Coari.

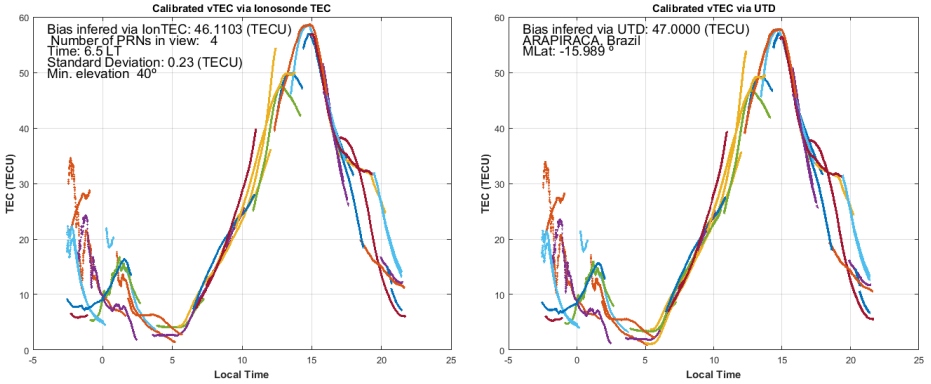

a

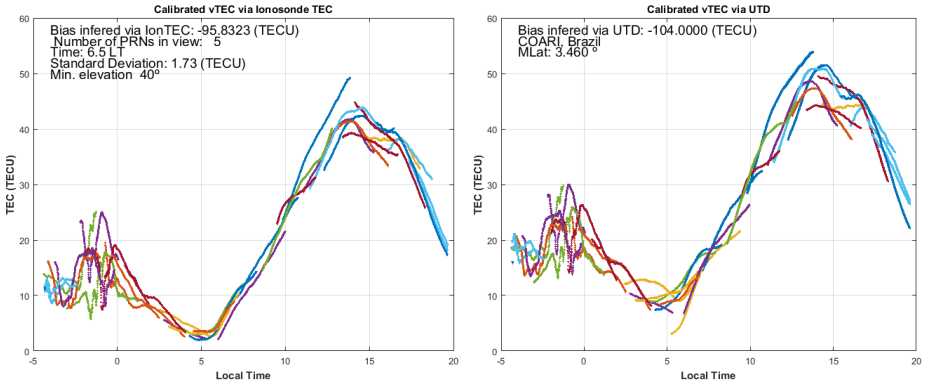

b

The same as Figures 4.3 and 4.4 for the stations of Arapiraca (a) and Coari (b). Such GNSS stations do note have ionosondes; the calibrations where made using the $IONTEC(M_{lat})$ function.

SOURCE: The author.

Figure 4.6 - Day-to-day variability of each receiver bias.

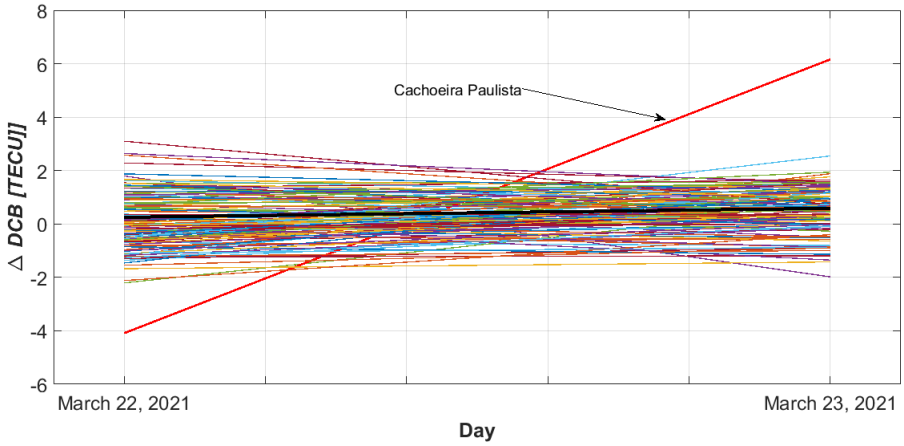

Day-to-day variability of the estimated receiver biases for the stations used in this work. The lines represent the stations, the vertical axis shows the difference between the bias estimated at the specific day minus the one estimated in the previous day. Also, the black line shows the average change.

SOURCE: The author.

Figure 4.7 - Uncalibrated $STEC$ and calibrated TEC for the Cachoeira Paulista station during the three days, 21, 22, and 23 of March, 2021.

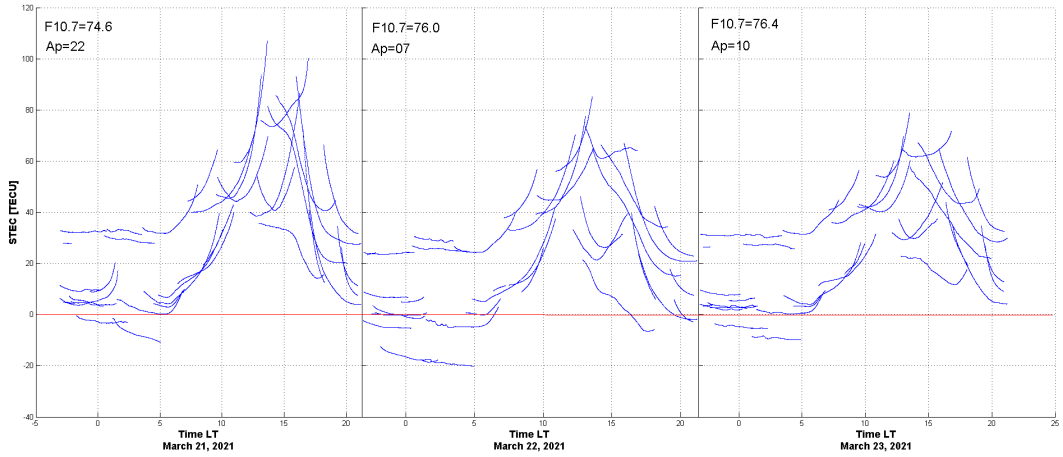

a

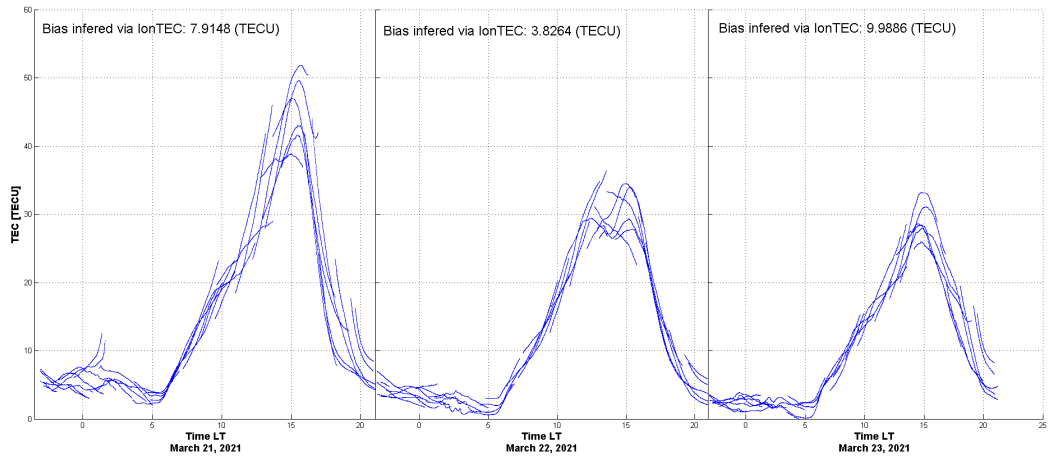

b

(a) slant TEC and (b) TEC calibrated by our method (blue lines) for Cachoeira Paulista station during Mach 21, 22, and 23, 2021. The horizontal red line is to show the zero point in the TEC scale.

SOURCE: The author.

Figure 4.8 - TEC map generated by $IONTEC$ method, all-sky imager and TEC by MAGGIA laboratory for Mach 21, 2021.

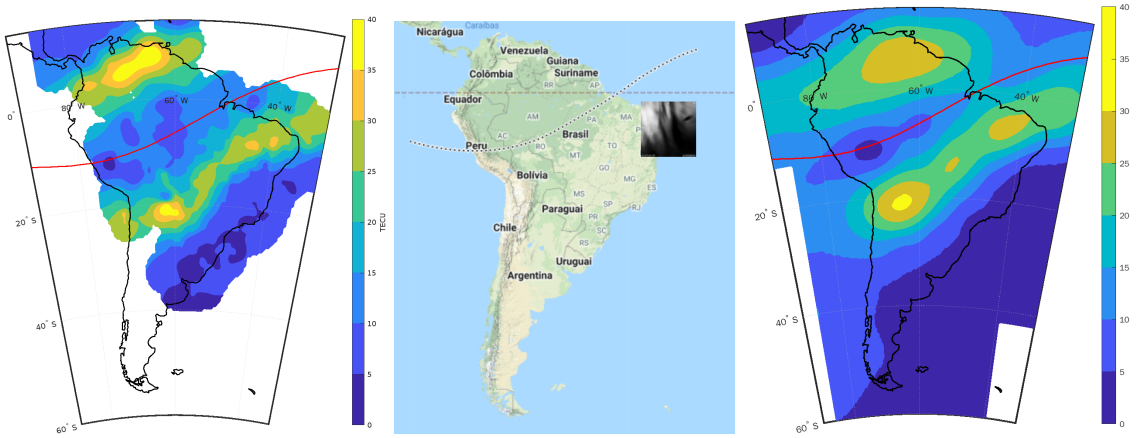

a b c

Maps for a qualitative comparison. The left panel (a) shows the TEC map obtained via $IONTEC$ method for 1:17 UT; the map at the center gives the information of the all-sky imager of São João do Cariri, obtained from Instituto Nacional de Pesquisas Espaciais (INPE) (2021) at the same time as (a); and the right panel shows the TEC map for 1:15 UT generated with data from MAGGIA laboratory (MENDOZA et al., 2020). The color bars of a and c are in $TECU$

SOURCE: (a) and (c), The author. (b), Instituto Nacional de Pesquisas Espaciais (INPE) (2021).

Figure 4.9 - TEC map generated by $IONTEC$ method, all-sky imager and TEC by MAGGIA laboratory for Mach 22, 2021.

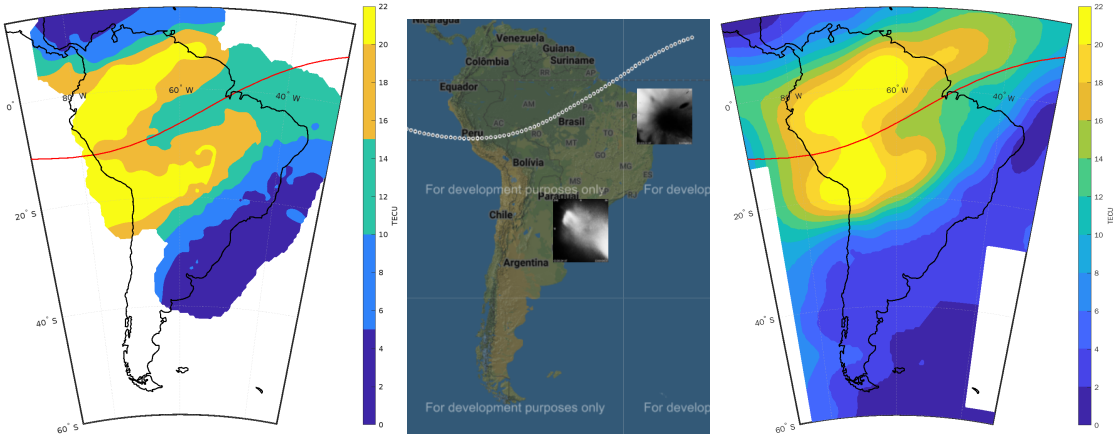

a b c

Maps for a qualitative comparison. The left panel (a) shows the TEC map obtained via $IONTEC$ method for 2:30 UT; the map at the center gives the information of the all-sky imager of São João do Cariri, obtained from Instituto Nacional de Pesquisas Espaciais (INPE) (2021) at the same time as (a); and the right panel shows the TEC map, also for 2:30 UT generated with data from MAGGIA laboratory (MENDOZA et al., 2020). The color bars of a and c are in $TECU$

SOURCE: (a) and (c), The author. (b), Instituto Nacional de Pesquisas Espaciais (INPE) (2021).

Figure 4.10 - *TEC* map generated by *IONTEC* method, all-sky imager and *TEC* by MAGGIA laboratory for Mach 23, 2021.

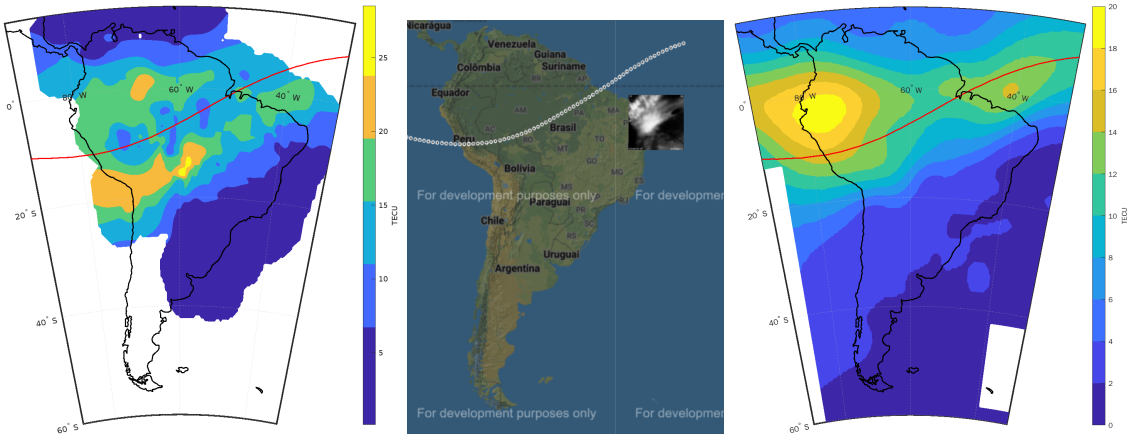

a b c

Maps for a qualitative comparison. The left panel (a) shows the *TEC* map obtained via *IONTEC* method for 3:00 UT; the map at the center gives the information of the all-sky imager of São João do Cariri, obtained from Instituto Nacional de Pesquisas Espaciais (INPE) (2021) at the same time as (a); and the right panel shows the *TEC* map, also for 3:00 UT generated with data from MAGGIA laboratory (MENDOZA et al., 2020). The color bars of a and c are in *TECU*

SOURCE: (a) and (c), The author. (b), Instituto Nacional de Pesquisas Espaciais (INPE) (2021).

Figure 4.11 - $S4$ indices for March 21-23, 2021.

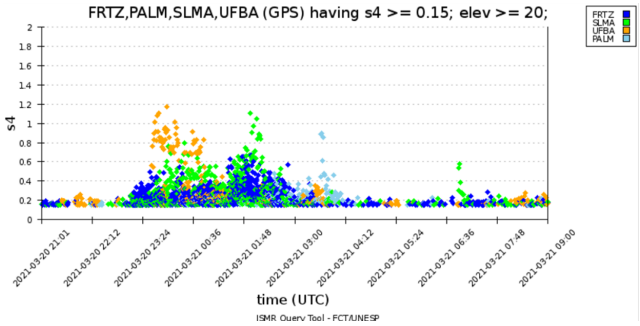

a

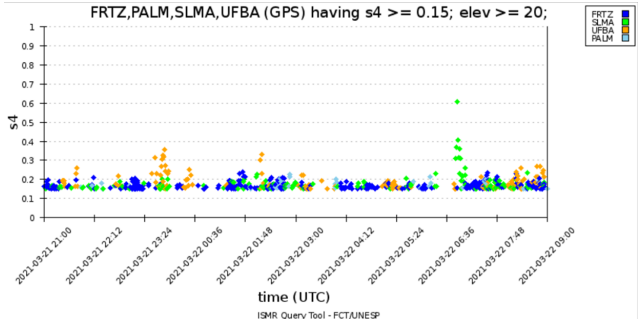

b

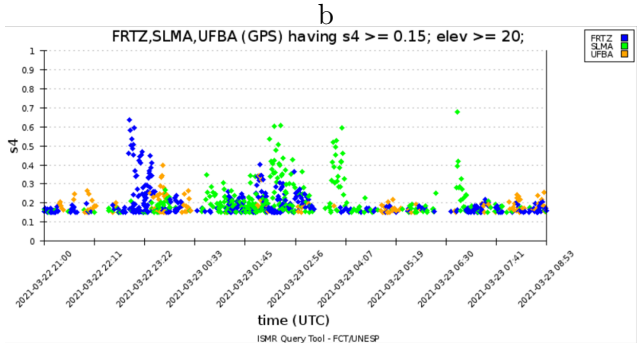

c

Scintillation index $S4$ for the stations in Fortaleza (blue), Palmas (cyan), Universidade Federal da Bahia (orange) and são Luís (green);on (a) March 21, 2021, (b) March 22, 2021, and (c) March 23, 2021. Also, in the pictures, are shown $S4 \geq 0.15$ from satellites with elevation angle $\geq 20°$.

SOURCE: Instituto Nacional de Ciência e Tecnologia (INCT) (2022).

5 CONCLUSIONS

We have developed a method for the Brazilian GNSS receivers calibration using ionosonde data. The approach consists in choosing a local time for ionosonde stations, at which the ionosphere is supposed to be approximately stable over each station and to have negligible longitudinal gradient over the Brazilian sector; then, an extrapolation criterion to complete the vertical electron density profile of the ionosonde up to 20,000 km, applying the adapted α-Chapman function and the full integration of such density to obtain the $IONTEC$, was used to calibrate the TEC data from these GNSS stations. The method was applied to the RBMC network stations for the days March 21-23, 2021 and the results were compared with the values obtained from the UTD code, where both showed good agreement. The impact of an arbitrary choice of the ionospheric height on the estimations of the receiver biases was analyzed. The results for heights of 250-450 km did not show relevant dependencies. The receiver biases variability for the selected three days were also investigated by calculating the average standard deviation; the obtained value is 0.6376 $TECU$. The anomalous case occurred at Cachoeira Paulista station, where a larger variation in the bias was noted and correctly detected by our method, ensuring the continuity of the TEC data series in a good way.

Also, the minimum curvature solution was employed in the calibrated TEC data to interpolate a function which describes the total electron content mainly over Brazil and it allows a comparison with maps produced by the MAGGIA laboratory. It is relevant to mention that our maps were able to identify ionospheric structures like EPB, unlike the MAGGIA maps. Such detection was strongly evidenced by fluctuations in the calibrated TEC plots, in All-Sky imager pictures, and scintillation index $S4$ analysis for the days used in this work.

However, some improvements are needed in the analysis. (1) to have more accurate results we need a more dense database, therefore, is necessary to expand the number of constellations, frequencies and networks (consequently the number of receivers) in order to cover a larger region. (2) The fitted $IONTEC$ function must be studied in different periods in order to investigate the possibility of building an empirical model to describe this in function of the day of the year and the $F10.7$ solar flux.

Some promising steps, which became feasible, after the development of this work include: (i) the development of an operational system for near real-time TEC calibration considering the receiver bias calculation every 24 hours or every 3 days, depending on the measurement stabilities; (ii) the development of threat models

used in air navigation applications, as well as an ionospheric background model for the SBAS system (*Satellite Based Augmentation System*); and, (*iii*) the production of IONEX (*IONosphere map EXchange*) (SCHAER et al., 1998) files. They are files with TEC values in a specific format, which allow the calculation of the positioning considering the single frequency signal.

REFERENCES

ABRAMOWITZ, M.; STEGUN, I. A.; ROMER, R. H. **Handbook of mathematical functions with formulas, graphs, and mathematical tables**. [S.l.]: American Association of Physics Teachers, 1988. 35

BALAN, N.; BAILEY, G. Equatorial plasma fountain and its effects: possibility of an additional layer. **Journal of Geophysical Research: Space Physics**, v. 100, n. A11, p. 21421–21432, 1995. 7

BALAN, N.; LIU, L.; LE, H. A brief review of equatorial ionization anomaly and ionospheric irregularities. **Earth and Planetary Physics**, v. 2, n. 4, p. 257–275, 2018. 7

BATISTA, I.; ABDU, M.; MACDOUGALL, J.; SOUZA, J. Long term trends in the frequency of occurrence of the F3 layer over Fortaleza, Brazil. **Journal of Atmospheric and Solar-Terrestrial Physics**, v. 64, n. 12-14, p. 1409–1412, 2002. 7

BITTENCOURT, J. A. **Fundamentals of plasma physics**. [S.l.: s.n.], 2004. 12, 13

CARRANO, C. S.; GROVES, K. M. The GPS segment of the AFRL-SCINDA global network and the challenges of real-time TEC estimation in the equatorial ionosphere. In: NATIONAL TECHNICAL MEETING OF THE INSTITUTE OF NAVIGATION, 2006. **Proceedings...** [S.l.], 2006. p. 1036–1047. 1, 20, 26, 28

HARGREAVES, J. K. **The solar-terrestrial environment: an introduction to geospace-the science of the terrestrial upper atmosphere, ionosphere, and magnetosphere**. [S.l.]: Cambridge University Press, 1992. 1, 7, 8, 9, 10, 11

HEIN, W. Z.; GOTO, Y.; KASAHARA, Y. Estimation method of ionospheric TEC distribution using single frequency measurements of GPS signals. **International Journal of Advanced Computer Science and Applications**, v. 7, n. 12, p. 1–6, 2016. 24

HOFMANN-WELLENHOF, B.; LICHTENEGGER, H.; WASLE, E. **GNSS–global navigation satellite systems: GPS, GLONASS, Galileo, and more**. [S.l.]: Springer Science & Business Media, 2007. 1, 5, 12, 16

INSTITUTO BRASILEIRO DE GEOGRAFIA E ESTATíSTICA (IBGE). **Rede brasileira de monitoramento contínuo dos sistemas GNSS (RBMC)**. 2021. Available from: <https://www.ibge.gov.br/>. Access in: 03 nov. 2021. 39

INSTITUTO NACIONAL DE CIêNCIA E TECNOLOGIA (INCT). **Tecnologia GNSS no suporte à navegação aérea (GNSS-NAvAer)**. 2022. Available from: <https://inct-gnss-navaer.fct.unesp.br/pt/>. Access in: 25 mar. 2022. 43, 53

INSTITUTO NACIONAL DE PESQUISAS ESPACIAIS (INPE). **Estudo e monitoramento brasileiro do clima espacial (EMBRACE)**. 2021. Available from: <http://www2.inpe.br/climaespacial/portal/pt/>. Access in: 03 nov. 2021. 2, 3, 42, 50, 51, 52

JAKOWSKI, N. Ionospheric GPS radio occultation measurements on board CHAMP. **GPS Solutions**, v. 9, n. 2, p. 88–95, 2005. 2, 29, 30

KELLEY, M. C. **The Earth's ionosphere: plasma physics and electrodynamics**. [S.l.]: Academic Press, 2009. 6

KIL, H.; SU, S.-Y.; PAXTON, L. J.; WOLVEN, B. C.; ZHANG, Y.; MORRISON, D.; YEH, H. Coincident equatorial bubble detection by TIMED/GUVI and ROCSAT-1. **Geophysical Research Letters**, v. 31, n. 3, 2004. 43

KIVELSON, M. G.; KIVELSON, M. G.; RUSSELL, C. T. **Introduction to space physics**. [S.l.]: Cambridge University Press, 1995. 8, 9

KLIPP, T. d. S.; PETRY, A.; SOUZA, J. R. de; PAULA, E. R. de; FALCÃO, G. S.; VELHO, H. F. de C. Ionosonde total electron content evaluation using international global navigation satellite system service data. In: ANNALES GEOPHYSICAE, 2020. **Proceedings...** [S.l.], 2020. v. 38, n. 2, p. 347–357. 29, 30

MA, G.; MARUYAMA, T. Derivation of TEC and estimation of instrumental biases from GEONET in Japan. In: ANNALES GEOPHYSICAE, 2003. **Proceedings...** [S.l.], 2003. v. 21, n. 10, p. 2083–2093. 22

MENDOZA, L. P.; MEZA, A. M.; PAZ, J. M. A. Near-real-time VTEC maps: new contribution for Latin America space weather. **Advances in Space Research**, v. 65, n. 9, p. 2235–2246, 2020. 3, 34, 35, 36, 50, 51, 52

MONICO, J. F. G. et al. The GNSS NavAer INCT project overview and main results. **Journal of Aerospace Technology and Management**, v. 14, 2022. 39

OLIVEIRA, C. B. A. d.; ESPEJO, T. M. S.; MORAES, A.; COSTA, E.; SOUSASANTOS, J.; LOURENCO, L. F. D.; ABDU, M. A. Analysis of plasma bubble signatures in total electron content maps of the low-latitude ionosphere: a simplified methodology. **Surveys in Geophysics**, v. 41, n. 4, p. 897–931, 2020. 34

OTSUKA, Y.; OGAWA, T.; SAITO, A.; TSUGAWA, T.; FUKAO, S.; MIYAZAKI, S. A new technique for mapping of total electron content using GPS network in Japan. **Earth, Planets and Space**, v. 54, n. 1, p. 63–70, 2002. 1

PAJARES, M. H.; ZORNOZA, J. M. J.; SUBIRANA, J. S. **GPS data processing: code and phase: algorithms, techniques and recipes**. [S.l.]: Centre de Publicacions del Campus Nord, UPC, 2005. 1, 5, 15, 16, 17, 19

PARKER, R. L. **Geophysical inverse theory**. [S.l.]: Princeton University Press, 1994. 2, 34, 35

PIMENTA, A.; BITTENCOURT, J.; FAGUNDES, P.; SAHAI, Y.; BURITI, R.; TAKAHASHI, H.; TAYLOR, M. J. Ionospheric plasma bubble zonal drifts over the tropical region: a study using OI 630nm emission all-sky images. **Journal of Atmospheric and Solar-Terrestrial Physics**, v. 65, n. 10, p. 1117–1126, 2003. 43

PRÖLSS, G. **Physics of the Earth's space environment: an introduction**. [S.l.]: Springer Science & Business Media, 2012. 1, 5, 6, 7, 8, 9, 10

RIDEOUT, W.; COSTER, A. Automated GPS processing for global total electron content data. **GPS Solutions**, v. 10, n. 3, p. 219–228, 2006. 1, 25, 27, 41, 42

RISHBETH, H. **Introduction to ionospheric physics**. [S.l.]: Academic Press, 1969. 5, 9, 10

ROYAL OBSERVATORY OF BELGIUM (ROB). **GNSS research group, ionosphere: tutorial**. 2008. Available from: <http://gnss.be/ionosphere_tutorial.php>. Access in: 01 nov. 2021. 14

SCHAER, S.; GURTNER, W.; FELTENS, J. IONEX: the ionosphere map exchange format version 1. In: IGS AC WORKSHOP, 1998, Darmstadt, Germany. **Proceedings...** [S.l.], 1998. v. 9, n. 11. 36, 56

SCOTTO, C.; PEZZOPANE, M.; ZOLESI, B. Estimating the vertical electron density profile from an ionogram: on the passage from true to virtual heights via the target function method. **Radio Science**, v. 47, n. 01, p. 1–6, 2012. 11, 25

SYSTèME D'OBSERVATION DU NIVEAU DES EAUX LITTORALES (SONEL). **Système d'Observation du Niveau des Eaux Littorales**. 2022. Available from: <https://www.sonel.org>. Access in: 20 apr. 2022. 39

THEMENS, D. R.; JAYACHANDRAN, P.; LANGLEY, R.; MACDOUGALL, J.; NICOLLS, M. Determining receiver biases in GPS-derived total electron content in the auroral oval and polar cap region using ionosonde measurements. **GPS Solutions**, v. 17, n. 3, p. 357–369, 2013. 1, 17, 20, 21, 26, 27, 28, 29

VIERINEN, J.; COSTER, A. J.; RIDEOUT, W. C.; ERICKSON, P. J.; NORBERG, J. Statistical framework for estimating GNSS bias. **Atmospheric Measurement Techniques**, v. 9, n. 3, p. 1303–1312, 2016. 1

WESSEL, P.; BECKER, J. Interpolation using a generalized Green's function for a spherical surface spline in tension. **Geophysical Journal International**, v. 174, n. 1, p. 21–28, 2008. 2, 34, 35, 36

WILSON, B. D.; MANNUCCI, A. J. Instrumental biases in ionospheric measurement derived from GPS data. 1993. 42

ZAPELLA, M.; OLIVEIRA, L. B.; HUNT, R. GPS and GLONASS constellations for better time synchronizing reliability. In: ANNUAL CONFERENCE FOR PROTECTIVE RELAY ENGINEERS (CPRE), 71., 2018. **Proceedings...** [S.l.], 2018. p. 1–7. 18

PUBLICAÇÕES TÉCNICO-CIENTÍFICAS EDITADAS PELO INPE

Teses e Dissertações (TDI)

Teses e Dissertações apresentadas nos Cursos de Pós-Graduação do INPE.

Notas Técnico-Científicas (NTC)

Incluem resultados preliminares de pesquisa, descrição de equipamentos, descrição e ou documentação de programas de computador, descrição de sistemas e experimentos, apresentação de testes, dados, atlas, e documentação de projetos de engenharia.

Propostas e Relatórios de Projetos (PRP)

São propostas de projetos técnico-científicos e relatórios de acompanhamento de projetos, atividades e convênios.

Publicações Seriadas

São os seriados técnico-científicos: boletins, periódicos, anuários e anais de eventos (simpósios e congressos). Constam destas publicações o Internacional Standard Serial Number (ISSN), que é um código único e definitivo para identificação de títulos de seriados.

Pré-publicações (PRE)

Todos os artigos publicados em periódicos, anais e como capítulos de livros.

Manuais Técnicos (MAN)

São publicações de caráter técnico que incluem normas, procedimentos, instruções e orientações.

Relatórios de Pesquisa (RPQ)

Reportam resultados ou progressos de pesquisas tanto de natureza técnica quanto científica, cujo nível seja compatível com o de uma publicação em periódico nacional ou internacional.

Publicações Didáticas (PUD)

Incluem apostilas, notas de aula e manuais didáticos.

Programas de Computador (PDC)

São a seqüência de instruções ou códigos, expressos em uma linguagem de programação compilada ou interpretada, a ser executada por um computador para alcançar um determinado objetivo. Aceitam-se tanto programas fonte quanto os executáveis.